JGR Oceans

RESEARCH ARTICLE
10.1029/2020JC016604

Multi-Timescale Analysis of Tidal Variability in the Indian Ocean Using Ensemble Empirical Mode Decomposition

Adam T. Devlin[1,2,3], **Jiayi Pan**[1,2,3], **and Hui Lin**[1,2]

[1]Key Laboratory of Poyang Lake Wetland and Watershed Research of Ministry of Education, Nanchang, China, [2]School of Geography and Environment, Jiangxi Normal University, Nanchang, China, [3]The Chinese University of Hong Kong, Shatin, New Territories, Hong Kong, China

Key Points:

- Tidal variability can be correlated to sea level variability in the Indian Ocean at multiple timescales
- Ensemble empirical mode decomposition can assist in the analysis of sparse-record tide gauges
- Improved diagnosis of tidal evolution and rising sea levels in this region is essential to future coastal planning and logistics

Supporting Information:

- Supporting Information S1

Correspondence to:
J. Pan,
panj@cuhk.edu.hk

Citation:
Devlin, A. T., Pan, J., & Lin, H. (2020). Multi-timescale analysis of tidal variability in the Indian Ocean using ensemble empirical mode decomposition. *Journal of Geophysical Research: Oceans*, *125*, e2020JC016604. https://doi.org/10.1029/2020JC016604

Received 15 JUL 2020
Accepted 11 NOV 2020

Abstract Ocean tides have been observed to be changing worldwide for nonastronomical reasons, which can combine with rising mean sea level (MSL) to increase the long-term impact to coastal regions. Tides can also exhibit variability at shorter timescales, which may be correlated with short-term variability in MSL. This short-term coupling may yield higher peak water levels and increased impacts of exceedance events that may be equally significant as long-term sea level rise. Previous studies employed the tidal anomaly correlation (TAC) method to quantify the sensitivity of tides to MSL fluctuations at long-period (>20 years) tide gauges in basin-scale surveys of the Pacific and Atlantic Ocean, finding that TACs exist at most locations. The Indian Ocean also experiences significant sea level rise and tidal variability yet has been less studied due to a sparse network of tide gauges. However, since the beginning of the 21st century, more tide gauges have been established in a wider geographical range, bringing the possibility of better estimates of tidal and MSL variability. Here, we improve the TAC approach, using the ensemble empirical mode decomposition (EEMD) method to analyze tidal amplitudes and sea level at multiple frequency bands, allowing a more effective use of shorter record tide gauges and better understanding of multiple timescales of tidal variability. We apply this approach to 73 tide gauges in the Indian Ocean to better quantify tidal variability in these under-studied regions, finding that the majority of locations exhibit significant correlations of tides and MSL.

Plain Language Summary The long-term evolution of tides occurs alongside the long-term rise in sea level, which has implications for the future of coastal communities. In addition, many locations show a short-term correlation between mean sea level (MSL) and tides, which may amplify total water levels, and lead to short-term flooding and inundation. The method of analyzing the correlations of MSL and tides ("tidal anomaly correlations," or TACs) has been employed in recent studies that analyzed Pacific and Atlantic Ocean data, with the majority of locations revealing significant correlations. This study modifies previous methods to analyze tide gauges in the Indian Ocean, which has classically been understudied due to a shortfall of useable data where many tide gauges are of short record. The new approach can isolate different forms of variability from a tide gauge (e.g., seasonal, yearly, and multiyear) and allow a separate analysis via the TAC method. This approach is applied to 73 locations in the Indian Ocean to show that most exhibit significant correlation of MSL to tides at multiple time scales. The results of this study will help to better understand the nature of tidal evolution under future scenarios of sea level rise and will help coastal planning.

1. Introduction

It has become clear in recent decades that ocean tides can exhibit changes that cannot be explained by astronomical factors (Müller et al., 2011; Woodworth, 2010). Long-term evolution in tides has been reported on global scales (Dangendorf et al., 2017; Haigh et al., 2014, 2020; Mawdsley et al., 2015) and on regional scales in both the Atlantic and Pacific Oceans (Feng et al., 2015; Jay, 2009; Müller, 2011; Rasheed & Chua, 2014; Ray, 2006, 2009; Ross et al., 2017; Zaron & Jay, 2014), with different effects observed in different areas of the world ocean. Mean sea level (MSL) has also shown a global increase (Church & White, 2006, 2011), at an estimated average rate of $+1.7 \pm 0.2$ mm yr^{-1} taken from tide gauge measurements during 1900–2009, and at $+3.4 \pm 0.4$ mm yr^{-1} for 1993–2016 as estimated from satellite altimetry (Nerem et al., 2010). This rise,

however, is not spatially constant, as some regions like the Western Pacific can see rates in excess of 10 mm yr^{-1} (Merrifield, 2009).

The risks of long-term sea level rise and tidal changes are further complicated by short-term correlations between sea level and tides. These correlated variabilities may increase the impact of extreme water level events, such as storm surge or nuisance flooding (Buchanan et al., 2017; Cherqui et al., 2015; Moftakhari et al., 2015, 2017, 2018; Ray & Foster, 2016; Sweet & Park, 2014). These short-term extrema may be hidden when analyzing only long-term linear trends yet are often equally important to understanding the risks and hazards to coastal zones, and changes in tidal components that amplify changes in sea level may have significant impacts to coastal defense networks (Pelling et al., 2013a, 2013b; Pelling, 2014). Locations which have a strong positive correlation in short-term fluctuations of tides and MSL can amplify flood risk beyond levels estimated by stationary tide assumptions, and may also suggest possible increased impacts of storm-induced flooding, since both tides and storm surge are long-wave processes (Arns et al., 2017; Familkhalili & Talke, 2016). Thus, both tides and MSL should be considered in concert at both long- and short-term timescales when determining the extent of future sea-level changes and associated flood scenarios, and understanding water level dynamics on a station-by-station basis can elucidate where tidal evolution will be a substantial addition to sea level rise.

The possible mechanisms for changes in MSL and tides involve numerous and interrelated nonastronomical reasons (Devlin et al., 2017a, 2017b). Tides can be directly modified by changes in water depth (Holleman & Stacey, 2014) or by other mechanisms that induce MSL change. Previous studies suggest that changes in the amplitude (or phase) of a tidal constituent may be a function of multiple variables:

$$\Delta \mathrm{Amp}_{\mathrm{tidal}} = f\left(\Delta H, \Delta Q_r, \Delta \rho, \Delta m_x, \Delta r, \Delta \Psi_\omega, \ldots\right) \quad (1)$$

where H is the water depth, ρ is the water density, r is the friction, m_x is the mixing, Q_r is the river discharge, and Ψ_ω represents the frequency-dependent tidal response to astronomical tidal forcing. The "..." indicates other possible variables, such as wind. Specific mechanisms include friction-altering changes in water depth (Arbic et al., 2009), resonance changes in harbor or semi-enclosed bay regions (Amin, 1983; Cartwright, 1972; Chernetsky et al., 2010; Familkhalili & Talke, 2016; Green, 2010; Jay et al., 2011; Vellinga et al., 2014), or stratification changes induced by increased upper-ocean warming (Domingues et al., 2008; Müller et al., 2012), which may also influence internal tides (Colosi & Munk, 2006; Müller, 2012). On a shorter timescale, seasonal tidal variations can be due to rapid changes in water column stratification (Kang et al., 1995; Müller, 2012), by annual wind-related cycles such as monsoons, by seasonal river flow characteristics (Godin, 1991; Guo et al., 2015), or by internal tide mixing (Sharples et al., 2007). Since many of the variables which affect sea level (river flow, density, and wind) can also affect tidal amplitudes, a correlated response is frequently observed. Additionally, locations which have a high sensitivity of tides to sea level changes also suggest possible increased impacts of storm-induced flooding, since both tides and storm surge are long-wave processes (Arns et al., 2017; Familkhalili & Talke, 2016). Figure 2 in Devlin et al. (2017a) showed a schematic of the possible mechanisms that can affect MSL and tides. In addition to these mechanisms, observed changes in the S_2 tide may be influenced by alterations in daily solar heating and irradiance (Arbic, 2005; Godin, 1986; Munk & Cartwright, 1966; Ray, 2001). The existence of multiple mechanisms, many of which may be correlated with each other, can make it difficult to determine the exact causes of observed variability. Yet, understanding these correlations is still vital, with the best strategy being to consider each location's dominating factors. No matter the exact cause of these changes, the consequences to coastal zones are due to total sea level, that is, the sum of MSL and time-variable water levels (including tides). The combinations of both of these changes will have an amplified impact to coastal zones in the coming century and beyond, with associated risks to ecosystems, coastal infrastructure and population centers.

1.1. Tidal Observations in the Indian Ocean

Tidal parameters and sea level rise have been studied extensively in the past in both the Atlantic and Pacific Oceans, as both basins have extensive observation networks of tide gauges, many of which have been recording water levels for 100 years or more. The Indian Ocean, however, is much sparser in its observational history. Compared with other basins, there are much fewer tide gauges, and most that

do exist have been recording for a short time and are concentrated in certain regions. This has made it difficult to conduct meaningful studies of long-term sea level rise, and even more difficult to understand tidal properties from tide gauges. There have been a few notable studies on sea level dynamics in the Indian Ocean (e.g., Church et al., 2006b; Han et al., 2010), but none have looked closely at tidal evolution on a basin scale.

Only three countries with shores on the Indian Ocean have established any major observational networks: Australia, South Africa, and India. Of these, only Australia's data is long-record, reliable, geographically well-distributed, and publicly available, and consequently, is also the most studied in terms of sea level and tides (Church et al., 2006a; Haigh et al., 2011; Watson, 2011; White et al., 2014). There are about a dozen South African tide gauges, and though most were established 50 years ago, all of them had operational issues or fell into disrepair near the end of the last century, and there is nearly no data available for the entire decade of the 1990s (Woodworth et al., 2007). All of these gauges were later recommissioned in the mid-2000s through ambitious projects to improve the tide gauge observations in the region, such as the ODINAfrica network (IO COMISSION, 2007), though it is unfortunate that what could have been very long and continuous records suffer from decadal data gaps, which makes estimates of sea level rise and tidal evolution more complicated. However, these new tide gauge network has begun to yield new and informative studies combining observations and numerical modeling in the South African region (e.g., Rautenbach et al., 2019).

India does have a significant number of long-record tide gauges, some of which have been recording for a 100 years or more. However, these hourly data are not publicly available due to concerns of propriety and security, and only limited monthly averaged sea level data are available for public study. Additionally, previous studies that did analyze historical Indian tide gauges found that only a handful could be considered fully reliable, since there were some historical issues with the operation of certain gauges, and other observations were complicated by natural factors such as extreme river discharge (Clarke & Liu, 1994; Emery & Aubrey, 1989). Some recent studies have made more progress studying sea level and tidal dynamics off the coast of India, but they are few in number (e.g., Shankar, 2000; Unnikrishnan, 2010; Unnikrishnan et al., 2006). This leaves a very under-sampled picture of most of the Indian Ocean, in particular with regard to tidal variability.

Though there is a shortfall of research literature about the oceanographic properties of the Indian Ocean, the situation has recently improved. One major event that has helped to improve the observational capabilities was the 2004 Sumatra megathrust earthquake. This quake and the resulting tsunami were devastating to the region, causing hundreds of thousands of deaths, displacing millions of people, and causing incalculable damage to coastal communities (Nagarajan et al., 2006). It was realized in the aftermath of this quake that the early warning capacity that tide gauges bring were severely lacking, and great effort was put forth by many countries to establish many new tide gauges across the region. Though the motivation for these new projects was a better monitoring of tsunamis, the same instruments have also brought new capabilities for the observations of tides and their relations to sea level variability. In addition, there have been networks of bottom pressure recorders installed in multiple deep-water locations as an early warning system for tsunamis; these instruments may also resolve tidal characteristics (Ray, 2013; Stammer et al., 2014). The advent of satellite altimetry and ocean modeling has also yielded an improved understanding about the large-scale and regional-scale features of tides in the Indian Ocean. Recent works have studied tides and sea level in certain areas of the Indian Ocean using numerical modeling and analytical methods based on altimetry observations, such as in the Arabian Sea and connected waters (Akbari et al., 2016), in the Persian Gulf (Kämpf & Sadrinasab, 2006; Pous et al., 2012) the Bay of Bengal (Dube et al., 2009; Sindhu, 2013), and in the Indonesian Seas (Robertson & Ffield, 2008).

The Indian Ocean also will have increasing importance to global trade and partnerships in coming years, as this is the planned route for the New Maritime Silk Road, part of China's ambitious “One Belt, One Road” initiative (Feng & Deng, 2018). The oceanic component of this endeavor will run from China through the South China Sea traveling west through the northern parts of the Indian Ocean, with termini in Africa and the Middle East. Thus, questions about the behavior of sea level and tides along this route are now a matter of practicality instead of simply scientific curiosity, as an increased knowledge and understanding will assist shipping logistics and construction of new coastal infrastructure.

1.2. Short-Term Correlations of Tidal and MSL Fluctuations and the TAC Method

Recent studies have quantified tidal sensitivity related to short-term sea level fluctuations via the tidal anomaly correlation (TAC) method (Devlin et al., 2017a, 2017b, 2019a, 2019b). A survey of 152 Pacific Ocean locations found that over 90% had significant correlations in at least one tidal constituent (Devlin et al., 2017a). A separate study of 170 Atlantic gauges found significance at 95% of locations (Devlin et al., 2019a). In a related work (Devlin et al., 2017b), the four largest tidal components were combined as a proxy for changes in the highest astronomical tide (δ-HAT), with 35% of gauges having a sensitivity of at least 50 mm to sea level fluctuations of 1 m (5% variability or more) in the Pacific Ocean, and over 50% in the Atlantic Ocean. The patterns of TACs show important regions of significance, such as Japan, the eastern coast of Australia, the South China Sea, along the United States east coast, in the North Sea, and the English Channel. Hong Kong exhibits an extremely strong positive tidal sensitivity, demonstrated in a focused regional study of multiple tide gauges (Devlin et al., 2019b). The TACs and δ-HATs can show a mixed signature; changes in tidal amplitudes can be positive or negative for a positive MSL fluctuation. Negative TACs indicate that a rising sea level may partially diminish the tides, whereas a positive TAC suggests a tidal amplification. It is the latter case (positive TACs or δ-HATs) that are most important to understand since these may directly increase total sea levels and may exceed stationary tide assumptions. Conversely, locations with negative TACs may see a reduced impact of total sea levels under situations of increasing MSL, though this situation merely gives a bit more time before the impacts of MSL rise will be felt. In all cases, accurate understanding of tidal sensitivity related to MSL changes is a critical concern for all coastal communities.

1.3. Improvement of the TAC Method via EEMD

The recent increase of tide gauge data in the Indian Ocean brings a new opportunity to make a meaningful study of MSL-related tidal variability. However, to carry out this study accurately, the TAC methods must be adapted to adjust to a sparse data inventory. In previous works by Devlin et al. (2014, 2017a, 2017b, 2019a, 2019b), the approach involved the analysis of hourly tide gauge data via harmonic analysis, using 1-year windows. The previous criteria for a minimum record length was ~20 years, as this gives 20 individual data points, allowing a sufficient regression analysis to be performed between tidal amplitudes and MSL. In the Pacific and Atlantic, there are numerous gauges that fulfill this requirement, but in the Indian, there are much less to choose from. Besides Australia, there are only about 12 publicly available gauges which have greater than 20 years of data, most of which are on islands. However, as there have been many new gauges established or re-established since 2004, there are now many gauges with ~10 years of useable data. Thus, if the 20-year record length requirement can be relaxed, then more locations can be analyzed.

The use of yearly harmonic analysis windows was suitable for previous works, in which the interest was the interannual behavior of the tides and MSL. However, higher frequency variability (monthly and seasonal) that will be constrained by a yearly analysis might also be of importance to the short-term behavior of tides, MSL, and total sea levels, particularly in response to weather events such as monsoons. Another limitation of the previous approach is that it did not differentiate what frequencies of variability are important, that is, whether the TAC represents a correlation that is strongest on an annual scale, seasonal scale, or multi-year scale. Therefore, improvements to the TAC method require two considerations. First, it should use a smaller harmonic analysis window (e.g., monthly), which would allow shorter records to be employed and more timescales of variability to be revealed. Second, it should be able to separate all relevant timescales of both tides and MSL so that the time series is not overwhelmed by the strongest modes of variability (such as the annual cycle), and can compare modes individually via the TAC method. These two improvements will allow a better determination of which forms of variability are most important to the overall behavior of total sea levels.

These requirements can be accomplished via an ensemble empirical mode decomposition (EEMD) analysis. This is based on the empirical mode decomposition method (EMD), which is a dyadic, mode-splitting, adaptive time-frequency data analysis method that can be applied to linear or nonlinear time-series (Huang et al., 1998). The EEMD method is an improvement on EMD, which involves sifting an ensemble of white noise-added signal and treats the mean as the true result (Wu & Huang, 2009). Finite, noninfinitesimal white noise is used to force the ensemble to exhaust all possible solutions in the sifting process, thus mak-

ing the different scale signals collapse into proper intrinsic mode functions (IMFs) dictated by the dyadic filter banks. The white noise is averaged out with a sufficient number of trials, and the only part which survives the averaging process is the signal, which is then treated as a physical meaningful answer, making it a "noise-assisted data analysis" function. With EEMD, one can separate scales naturally without any *a priori* subjective criteria. An EMD-based approach has been previously shown to be able to separate tidal signals from hourly tide gauge records as a replacement for classical harmonic analysis methods (Cheng et al., 2017), though in our approach, we will apply EEMD to tidal determinations found after harmonic analysis has been performed.

1.4. Approach of This Study

This study will apply the EEMD method to all available tide gauge data in the Indian Ocean to better understand all timescales of tidal variability associated with MSL variability and determine any apparent basin-scale or regional patterns and discuss possible mechanisms for the observations. The rest of this study will be structured as follows. First, a description of the spatial and temporal coverage of the available data will be detailed. Next, the methodology of the TAC method using tidal admittances will be described as well as the use of EEMD to separate modes of variability. After this, results will be disseminated, followed by discussions and, finally, conclusions and future steps.

2. Methods

2.1. Data Inventory

All data in this study are acquired from two sources. Most of the data are acquired from the University of Hawai'i sea level center (UHSLC, uhslc.soest.hawaii.edu/) and remainder is from the Global Extreme Sea Level Analysis data set, 2nd edition (GESLA, Woodworth et al., 2016; www.gesla.org) archiving project, which includes data from the "public" archive as well as from a "private" archive for certain Australian gauges curated by John Hunter, to which access permission was granted. Using both data sources, the longest possible data record was patched together at each location. Typically, UHSLC was checked first, as this is the most frequently updated source, and GESLA was used to supplement our archive at locations not held by UHSLC. Figure 1 shows the entire domain, with locations of tide gauges indicated as red markers. Six locations in the open ocean as well as four locations in Antarctica are indicated by name. For a closer view of the rest of the ocean, four regions are delineated for a close-up view, as shown by the outlined boxes in Figure 1. First, region (a) covers the Arabian Sea region including the Red Sea, the Persian Gulf, and the Gulfs of Aden and Oman, with a total of eight locations. There is one location on the Horn of Africa (Djibouti), one location in Yemen (Aden), three locations in Oman (Salalah, Masiriah, and Muscat), one location in Bahrain (Mina Sulman), and one location in Pakistan (Karachi). Next, region (b) covers the Bay of Bengal region including the Andaman Sea with a total of 16 tide gauge locations. This includes three locations in the Maldives, four in Bangladesh, one in Sri Lanka (Colombo), one in India (Vishakhapatnam), one in Myanmar (Moulmein), one in Thailand (Ko Tapho Noi), three in Indonesia, and two other island locations, Diego Garcia Island (UK) and Cocos Island (Australia). Third, region (c) consists of the coast of Africa south of the Equator, which includes a total of 13 locations; eight in in South Africa (some of which are technically on the Atlantic Coast), one location in Tanzania (Zanzibar), and two in Kenya (Mombasa and Lamu). Finally, region (d) covers the western and southern coasts of Australia (21 gauges), and nearby locations in Indonesia (five gauges). There is a high concentration of tide gauges in some parts of southern Australia, such as near Adelaide and Williamstown, and exact locations are indicated by the arrows. Adelaide has two long-record tide gauges, one in the inner harbor and one in the outer harbor, which cover approximately the same time period. These regions, and the tide gauge locations are indicated in Figures 2a–2d.

The nature of EEMD analyses makes the results extremely sensitive to edge effects and large data gaps. Therefore, in some locations, such as for the South African tide gauges, which were nonoperational in the 1990s and 2000s, we will divide the useable data into "A" and "B" data sets and analyze them separately. A few other locations, such as Karachi and Colombo, have long gaps between the early and recent data, and others, such as Reunion Island, and Sibolga, Indonesia have had instrumental changes or relocations and two data sets are provided in the original source data. One location in Australia is a combination of two

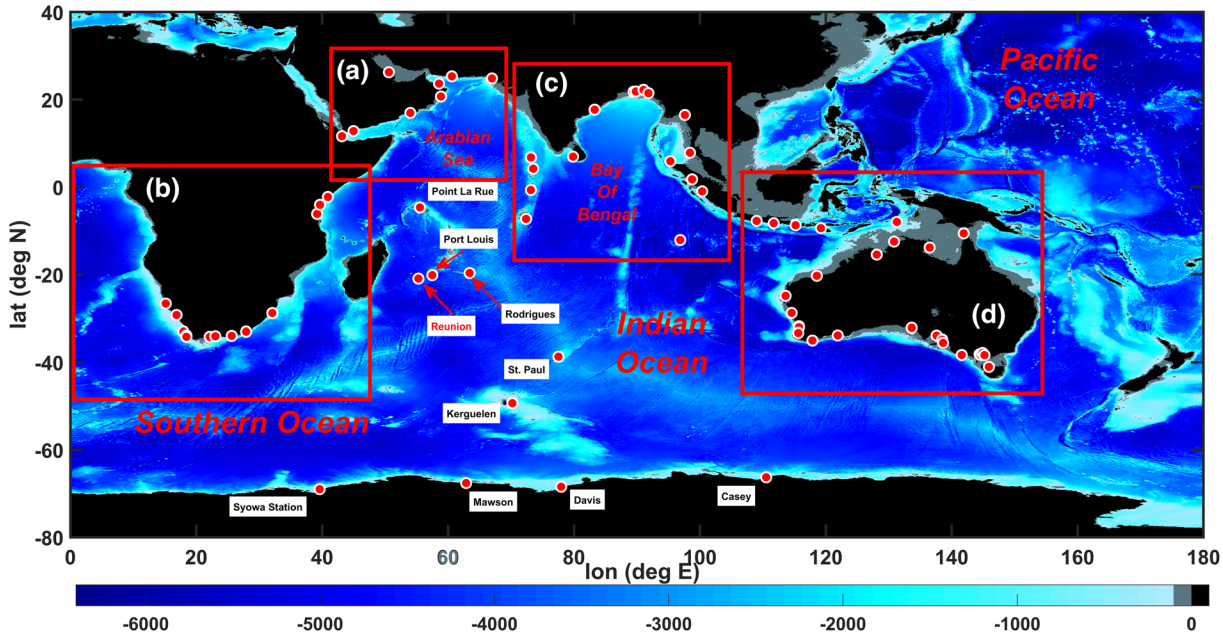

Figure 1. Tide gauge locations used in this study, indicated by red dots. Subdomains are outlined in red and labeled (a) through (d), corresponding to each subplot in Figure 2. Locations are named where outside of the four subdomains (central Indian Ocean and Antarctica). Stations named in red text have two separately analyzed data sets ("A" and "B"). Water depth is shown as the background according to the color bar at the bottom (units of meter).

separate records (earlier and recent) which are very near to each other (Milner Bay/Groote Eylandt). All these locations will also be split into "A" and "B" data sets. In Figures 1 and 2, locations which are split into multiple data sets will be indicated by red text. In addition to avoiding errors in the EEMD analysis, this approach will also have the benefit of providing a "before" and "after" picture of tidal variability and give insights into locations where tidal properties may have shifted over time. We update tide gauges as much as possible to make our determinations reflect the current situation of tidal variability, though there are some limitations. Most notably, the data in Bangladesh are somewhat out of date, as these locations have not been updated since the early 2000's (or 1992 in the case of Charchanga), Mina Sulman in Bahrain only runs from 1981 to 1997, and the Antarctic tide gauges have not been updated for about 10 years. In addition, many of the locations in Australia are only current to 2014 or 2016. We still elect to use the outdated data, however, since there is such a spatial limitation of available tide gauges in the Indian Ocean. In total, there are 73 unique tide gauge locations, and 15 of these are split into "a" and b" records, so there will be a total of 88 data sets analyzed. The details of each record, including name, country, latitude, longitude, time period analyzed, and data source are provided in Table 1.

2.2. Harmonic Analysis and Tidal Admittance Processing of Tide Gauge Data

Investigations of tidal perturbations are carried out using tidal admittances (Devlin et al., 2017a), the unitless ratio of an observed tidal constituent to its corresponding astronomical tidal potential. The use of a tidal admittance has the benefit of constraining and removing long-period cycles present in tide gauge records, such as the 18.61-year nodal cycle (Haigh et al., 2011), which may complicate tidal variability calculations. Monthly (32-day window) harmonic analyses are performed on hourly observed tidal records and the corresponding hourly tidal potential generated at the same location and time period, using the R_T_Tide tidal harmonic analysis package in MATLAB (Leffler & Jay, 2009; Pawlowicz et al., 2002). A separate code package transcribed from FORTRAN to MATLAB is used to generate the tidal potential (Cartwright & Tayler, 1971). The monthly harmonic analysis windows are then advanced 7 days and re-run until the end of the data record is reached. The result from each harmonic analysis determines an amplitude, A, and phase, θ, at the central time of the analysis window for each tidal constituent, with corresponding error estimates.

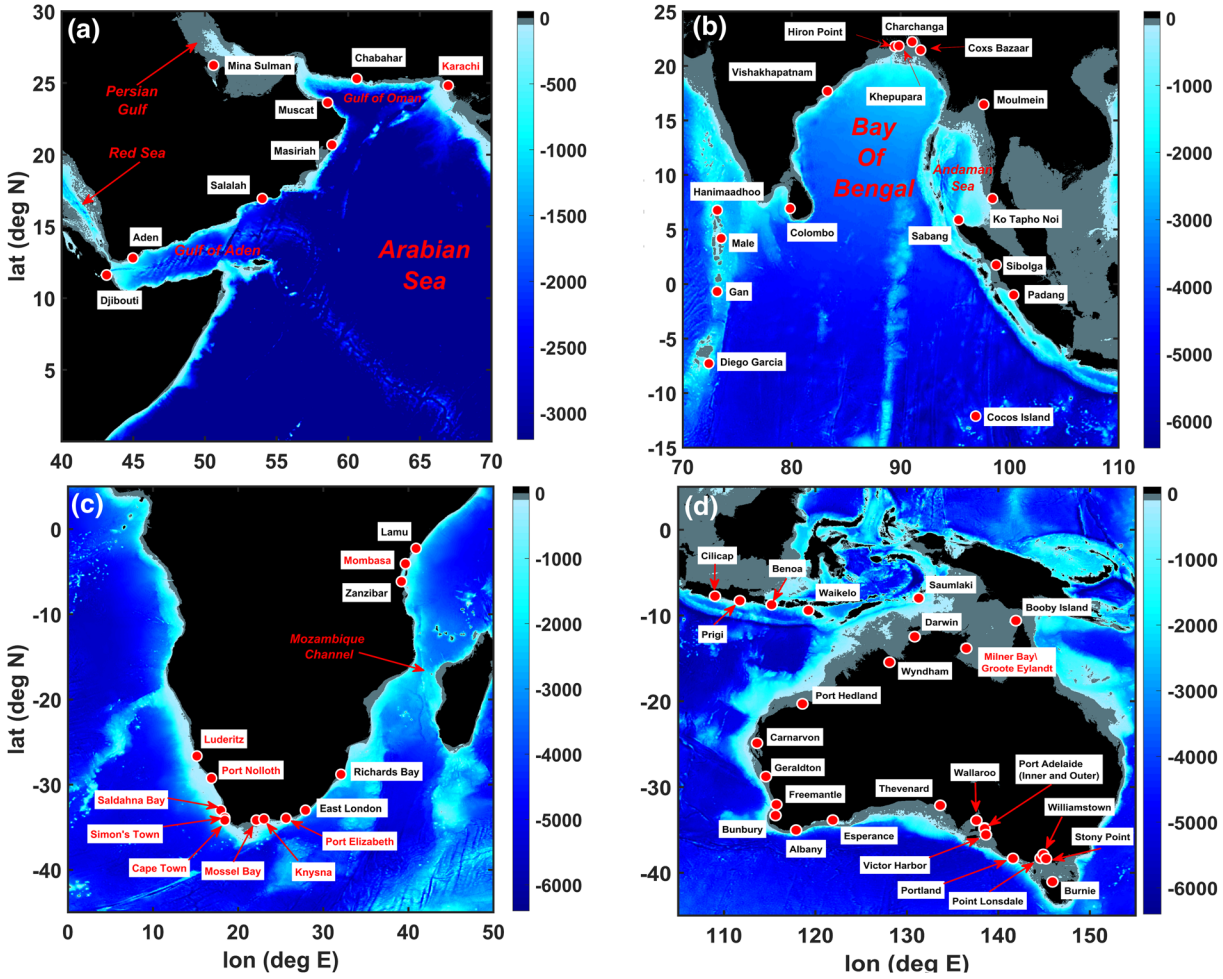

Figure 2. Close-up view of subdomains indicated in Figure 1 with station names indicated. Region (a) include the Middle East and Arabian Sea locations, region (b) includes southern African locations, region (c) includes Bay of Bengal locations, and region (d) includes Australian locations. Stations named in red text have two separately analyzed data sets ("A" and "B"). Water depth is shown as the background according to the color bar at the right (units of meter).

Use of this moving analysis window produces a running time-series of amplitude and phase. From amplitude $A(t)$ and phase $\theta(t)$ time series, one can construct complex amplitudes $\mathbf{Z}(t)$ through:

$$\mathbf{Z}(t) = A(t)e^{i\theta(t)} \tag{2}$$

The tidal admittance amplitude ($\mathbf{A}$) and phase lag ($\mathbf{P}$) for a constituent can be formed using Equations 3 and 4:

$$\mathbf{A}(t) = \mathrm{abs}\left|\frac{Z_{\mathrm{obs}}(t)}{Z_{\mathrm{pot}}(t)}\right| \tag{3}$$

$$\mathbf{P}(t) = \theta_{\mathrm{obs}}(t) - \theta_{\mathrm{pot}}(t), \tag{4}$$

where the subscript "obs" or "pot" denotes either the observed data or the gravitational potential, respectively. In this study, we will only consider the admittance amplitudes, as phase difference determinations based on monthly harmonic analyses will be highly variable and difficult to interpret physically. This process will be applied to the four largest tidal constituents; the M_2 and S_2 semidiurnal tides and the K_1 and O_1 diurnal

Table 1
Tide Gauge Locations of the Indian Ocean Used in This Study, Separated by Sub-Regions Following the Discussion in the Text

Station name	Region/country	Start year	End year	Sta. years	Latitude	Longitude	Source
Arabian Sea region							
Djibouti	Djibouti	2007	2016	9	11.61	43.14	UHI
Aden	Yemen	2008	2015	7	12.79	44.98	UHI
Salalah	Oman	1992	2015	23	16.94	54.01	UHI
Masiriah	Oman	1996	2017	21	20.69	58.87	UHI
Muscat	Oman	2009	2019	10	23.63	58.57	UHI
Mina Sulman	Bahrain	1981	1997	16	26.23	50.60	UHI
Chabahar	Iran	2007	2017	10	25.30	60.60	UHI
Karachi “A”	Pakistan	1985	1994	9	24.81	66.98	UHI
Karachi “B”	Pakistan	2007	2018	11	24.81	66.98	UHI
Bay of Bengal region							
Diego Garcia	UK	2006	2019	13	−7.29	72.39	UHI
Gan	Maldives	1991	2019	28	−0.69	73.15	UHI
Male	Maldives	1990	2019	29	4.19	73.53	UHI
Hanimaadhoo “A”	Maldives	1992	2002	10	6.77	73.17	UHI
Hanimaadhoo “B”	Maldives	2006	2019	13	6.77	73.17	UHI
Colombo “A”	Sri Lanka	1953	1965	12	6.93	79.85	UHI
Colombo “B”	Sri Lanka	2006	2019	13	6.93	79.85	UHI
Cocos Island	Australia	1985	2016	31	−12.12	96.88	UHI
Hiron Point	Bangladesh	1977	2003	26	21.78	89.47	UHI
Khepupara	Bangladesh	1987	2000	13	21.83	89.83	UHI
Charchanga	Bangladesh	1980	1992	12	22.22	91.05	UHI
Coxs Bazaar	Bangladesh	1983	2002	19	21.45	91.83	UHI
Moulmein	Myanmar	2012	2019	7	16.47	97.62	UHI
Vishakhapatnam	India	2011	2019	8	17.68	83.28	UHI
Ko Tapho Noi	Thailand	1985	2019	34	7.83	98.43	UHI
Sabang	Indonesia	2006	2017	11	5.89	95.32	UHI
Sibolga “A”	Indonesia	1989	2000	11	1.75	98.77	UHI
Sibolga “B”	Indonesia	2005	2017	12	1.75	98.77	UHI
Padang	Indonesia	2006	2017	11	−1.00	100.37	UHI
African region							
Luderitz “A”	South Africa	1961	1990	29	−26.65	15.15	GPUB
Luderitz “B”	South Africa	2008	2015	7	−26.65	15.15	GPUB
Port Nolloth “A”	South Africa	1959	1989	30	−29.25	16.87	GPUB
Port Nolloth “B”	South Africa	2004	2016	12	−29.25	16.87	GPUB
Saldahna Bay “A”	South Africa	1983	1994	11	−33.02	17.95	GPUB
Saldahna Bay “B”	South Africa	2000	2011	11	−33.02	17.95	GPUB
Cape Town “A”	South Africa	1967	1990	23	−33.90	18.43	GPUB
Cape Town “B”	South Africa	2004	2018	14	−33.90	18.43	GPUB
Simon's Town “A”	South Africa	1959	1988	29	−34.18	18.43	UHI
Simon's Town “B”	South Africa	2003	2016	13	−34.18	18.43	UHI
Mossel Bay “A”	South Africa	1974	1993	19	−34.18	22.13	GPUB
Mossel Bay “B”	South Africa	2006	2018	12	−34.18	22.13	GPUB

Table 1
Continued

Station name	Region/country	Start year	End year	Sta. years	Latitude	Longitude	Source
Knysna "A"	South Africa	1966	1988	22	−34.05	23.03	GPUB
Knysna "B"	South Africa	2006	2018	12	−34.05	23.03	GPUB
Port Elizabeth "A"	South Africa	1978	1989	11	−33.96	25.63	UHI
Port Elizabeth "B"	South Africa	2000	2018	18	−33.96	25.63	UHI
East London	South Africa	2004	2018	14	−33.02	27.92	GPUB
Richards Bay	South Africa	2000	2018	18	−28.80	32.08	GPUB
Zanzibar	Tanzania	1984	2018	34	−6.16	39.19	UHI
Mombasa "A"	Kenya	1986	2005	19	−4.07	39.66	UHI
Mombasa "B"	Kenya	2006	2018	12	−4.07	39.66	UHI
Lamu	Kenya	1995	2018	23	−2.27	40.90	UHI
Australian region							
Cilicap	Indonesia	2007	2017	10	−7.75	109.02	UHI
Prigi	Indonesia	2007	2017	10	−8.28	111.73	UHI
Benoa	Indonesia	2006	2017	11	−8.75	115.21	UHI
Saumlaki	Indonesia	2008	2017	9	−7.98	131.29	UHI
Waikelo	Indonesia	2008	2018	10	−9.40	119.23	UHI
Booby Island	Australia	1989	2019	30	−10.60	141.92	UHI
Milner Bay ("A")	Australia	1972	1986	14	−13.83	136.50	GPRI
Groote Eylandt ("B")	Australia	1993	2014	21	−13.83	136.50	UHI
Darwin	Australia	1986	2016	30	−12.47	130.85	UHI
Wyndham	Australia	1975	2014	39	−15.45	128.10	GPRI
Port Hedland	Australia	1988	2014	26	−20.30	118.58	UHI
Carnarvon	Australia	1990	2014	24	−24.88	113.62	UHI
Geraldton	Australia	1984	2014	30	−28.78	114.58	GPRI
Freemantle	Australia	1984	2014	30	−32.05	115.73	UHI
Bunbury	Australia	1984	2014	30	−33.32	115.63	GPRI
Albany	Australia	1984	2014	30	−35.03	117.88	GPRI
Esperance	Australia	1986	2016	30	−33.87	121.90	UHI
Thevenard	Australia	1986	2016	30	−32.15	133.65	UHI
Wallaroo	Australia	1983	2014	31	−33.90	137.60	GPRI
Port Adelaide (Outer)	Australia	1984	2014	30	−34.78	138.48	GPRI
Port Adelaide (Inner)	Australia	1984	2014	30	−34.85	138.50	GPRI
Victor Harbor	Australia	1984	2014	30	−35.57	138.63	GPRI
Portland	Australia	1982	2016	34	−38.33	141.60	UHI
Point Lonsdale	Australia	1984	2014	30	−38.30	144.62	GPRI
Williamstown	Australia	1983	2013	30	−37.87	144.92	UHI
Stony Point	Australia	1983	2014	31	−38.37	145.22	GPRI
Burnie	Australia	1985	2015	30	−41.05	145.92	UHI
Indian Ocean Islands							
Port Louis	Mauritius	1986	2019	33	−20.16	57.50	UHI
Rodrigues	Mauritius	1990	2019	29	−19.67	63.42	UHI
Reunion "A"	France	1996	2006	10	−20.94	55.29	UHI
Reunion "B"	France	2007	2019	12	−20.94	55.29	UHI

Table 1
Continued

Station name	Region/country	Start year	End year	Sta. years	Latitude	Longitude	Source
Point La Rue	Seychelles	1993	2019	26	−4.67	55.53	UHI
St. Paul	France	1994	2006	12	−38.71	77.54	UHI
Kerguelen	France	1993	2012	19	−49.35	70.22	UHI
Antarctica							
Syowa Station	Japan	1990	2013	23	−69.00	39.60	UHI
Mawson	Australia	1992	2009	17	−67.60	62.87	UHI
Davis	Australia	1993	2010	17	−68.45	77.97	UHI
Casey	Australia	1996	2008	12	−66.28	110.53	UHI

Note. Each location indicates station name, country of ownership, start year, end year, total amount of station-years used, latitude, longitude, and primary data source (UHI, University of Hawaii Sea Level Center; GPUB, GESLA public archive; GPRI, GESLA private archive). A number of locations have two separately analyzed data sets, so two records are indicated.

tides. We also consider a proxy for the change in the δ-HAT by combining the time series of these four tides, typically 75% of the full tidal range. MSL time-series are also generated by the harmonic analysis code.

There are, however, some limitations inherent to using monthly analysis methods that much be mentioned here. Not as many tidal constituents can be resolved in a monthly analysis (~35) as can in a yearly analysis (~70), and some smaller constituents may "leak" into other dominant tidal components during the HA process, such as the P_1 tide, which can leak into the K_1 constituent signal. The K_2 tide can also not typically be resolved. However, both of these tidal components are generally small magnitude, so it should not influence the results much. Another concern is that the S_2 tide is partially influenced by solar-related atmospheric pressure forcing (about 15% in general), which is not corrected for in our study, and may be an complicating factor to the tidal admittance methods at some locations in our study, especially at locations on or near the equator where solar radiation is prevalent (Ray, 2009). In yearly analyses, some of the seasonal variability of the solar pressure forcing cycle may be constrained, but in monthly analyses, it may be more prevalent, as any solar-related cycle will likely influence and possibly complicate any seasonal-scale tidal variability. However, we assume that this effect is not significant enough to affect the final results. Since we are limited by the shortness of the tide gauge records in the Indian Ocean, yearly analyses are simply not practical to use at present to understand tidal variability, so we merely mention these caveats here, and any instances where these complicating factors might have influenced our results are mentioned in the Section 4.

2.3. Application of EEMD to MSL and Tidal Data

After harmonic analysis, all variables are examined for continuity. Small gaps (a few months or less) in the results will need to be filled by a definite number since NaN values cannot be used in the EEMD calculations, we therefore calculate the average value of the variable, and fill the gaps with this average value. This does not influence the calculation of the modes if the gaps are small. All input variables (sea level and tides) will be conditioned for comparison via the use of EEMD, which analyzes each time series and splits it into several modes of variability called IMFs. The lowest frequency IMF will give the long-term trend, while the higher IMFs will contain high-frequency variability. Each set of MSL and tidal data will be split into eight IMFs. We will remove the highest frequency IMF to constrain noise, and will also remove the lowest IMF since we are not concerned here with the long-term trend, as the majority of our locations are short records, so any estimates of long-term change will not be statistically robust. Thus, our main concern in this study will be IMFs 2–7. The middle IMFs (4 and 5) will be of particular interest as these will capture the yearly variability that is related to climate cycles such as the monsoon.

2.4. TAC and δ-HAT Analysis

Tidal sensitivity to sea-level fluctuations is quantified using TACs, the relationships of detrended tidal variability to detrended MSL variability. We determine the sensitivity of the tidal admittance to MSL pertur-

bations by calculating regressions between MSL and individual tidal admittances taken from the EEMD process as well as for δ-HATs, considering single IMFs as well as combinations of IMFs. The slope of the regression will be the TAC or δ-HAT, and regression statistics will give an estimate of the error, expressed in units of millimeter change in tidal amplitude per 1-m fluctuation in sea-level (mm m^{-1}). Significant results are defined as those whose slope is more than twice the associated error, that is, a signal-to-noise ratio (SNR) greater than 2.0, though we will strive to use determinations greater than this wherever possible. For most records, we will use the full data record, as the majority are short (8–15 years). Some gauges in Australia have a longer record of 50 years or more. However, previous works showed TACs may be dependent on record length and may even change over time (Devlin 2017a, 2017b), therefore, for the longer record gauges, we will only calculate TACs over the last 30 years of the record to provide consistency with other short record locations.

The frequency of each mode can be estimated by using code in the EEMD software to determine time series of the instantaneous frequency (IF) of each IMF. For the majority of tide gauge records, the sifting process of the IMFs yields slightly different IFs in MSL as compared to the corresponding modes in tidal admittances. For example, in most MSL records, an annual mode of ~1 cycle per year is usually found in IMF #4, but tidal properties have an annual mode that can be found in either IMF #4 or #5, or slightly offset from a true annual frequency (e.g., IMF#4 of some tides may be ~0.75 cycle per year and IMF# 5 may be ~1.2 cycle per year). Therefore, we will sometimes need to combine modes of tides to find the best correlation to the MSL IMF considered. Hereafter, we will use a shorthand notation to write these comparisons, of the form: MSL_4 versus X_4, versus X_5, versus $X_{4/5}$, and so on, where the subscript indicates the IMF mode, and "X" will indicate the tidal admittance of the relevant tidal component (e.g., K_1, M_2, S_2, O_1, or HAT). The comparisons will be based on the MSL IMFs, and will consider three comparisons to each MSL IMF, of the form: MSL_i versus X_i, MSL_i versus X_{i+1}, and MSL_i versus $X_i + X_{(i+1)}$ where $i = 2,3,4,5,6$; that is, IMF #4 of MSL will be compared with X_4, X_5, and X_{4+5}. In practice, MSL_7 and X_7 tend to be of exceedingly small magnitude, so these comparisons will be omitted from consideration. These comparisons will be categorized into three generalized frequency bands: (1) a sub-annual (SA) band, with frequencies usually between 0.1 and 0.75 years/cycles, corresponding to MSL_2, or MSL_3; (2) an annual (ANN) band, with frequencies generally between 0.75 and 1.25 years/cycle, corresponding to MSL_4; (3) an interannual (IA) band with frequencies between 1.5 and 8.0 years/cycle, corresponding to MSL_5 or MSL_6. After all comparisons are made, the best fit is chosen within each of the three frequency bands based on which combination has the strongest TAC or δ-HAT and the largest SNR.

We now illustrate the TAC process via EEMD using data from Wyndham, Australia as an example, which is a longer-record gauge with strongly positive IMFs. Figure 3 displays the EEMD breakdown of the data. The top left panel (a) shows the original data of MSL (red lines) and the K_1 admittance amplitude (blue lines), and the rest of the panels (b–i) show each IMF (1–8) of both data sets. It can be seen that many IMFs appear to have some measure of correlation with each other, especially the middle (annual) modes. Figure 4 better demonstrates the EEMD separation and comparison process. We consider the annual variation, taking the fourth mode of MSL as the basis (MSL_4). We then perform a comparison of MSL_4 with $K1_4$, $K1_5$, and $K1_{4+5}$ and find which is the "best" fit. Each time series comparison is shown in panels (a, c, and e). For visual convenience, we have zoomed in on the data and show only the past 15 years of the original data are shown in Figure 3. In panels (b, d, and f), we display the corresponding regression of MSL versus K_1 for each mode comparison; the original data in shown as black points, and the green line is the robust regression fit, the slope of which is the TAC value, with associated error. All three comparisons yield a visually good fit to each other, but the comparison of MSL_4 with $K1_{4+5}$ appears to be the best fit. This is numerically confirmed by the regressions, as this combination yields the largest TAC value (+288 ± 16 mm m^{-1}) and the highest SNR (18.0). Thus, this is our chosen comparison for the ANN band.

Table 2 shows a matrix of mode comparisons chosen, with the MSL IMFs on the *y*-axis, and the K_1 IMFs on the *x*-axis each of the three bands indicated by different colored regions of the table (SA, yellow; ANN, orange; IA, green). The TAC values for the K_1 tide at Wyndham, Australia are given along with errors in units of millimeter m^{-1}, along with SNRs shown in parentheses. Significant mode comparisons (i.e., SNR > 2.0) are italicized, and the best fit in each band is in bold text. This process is carried out for each data record and for each tidal component (K_1, M_2, S_2, O_1, and δ-HAT).

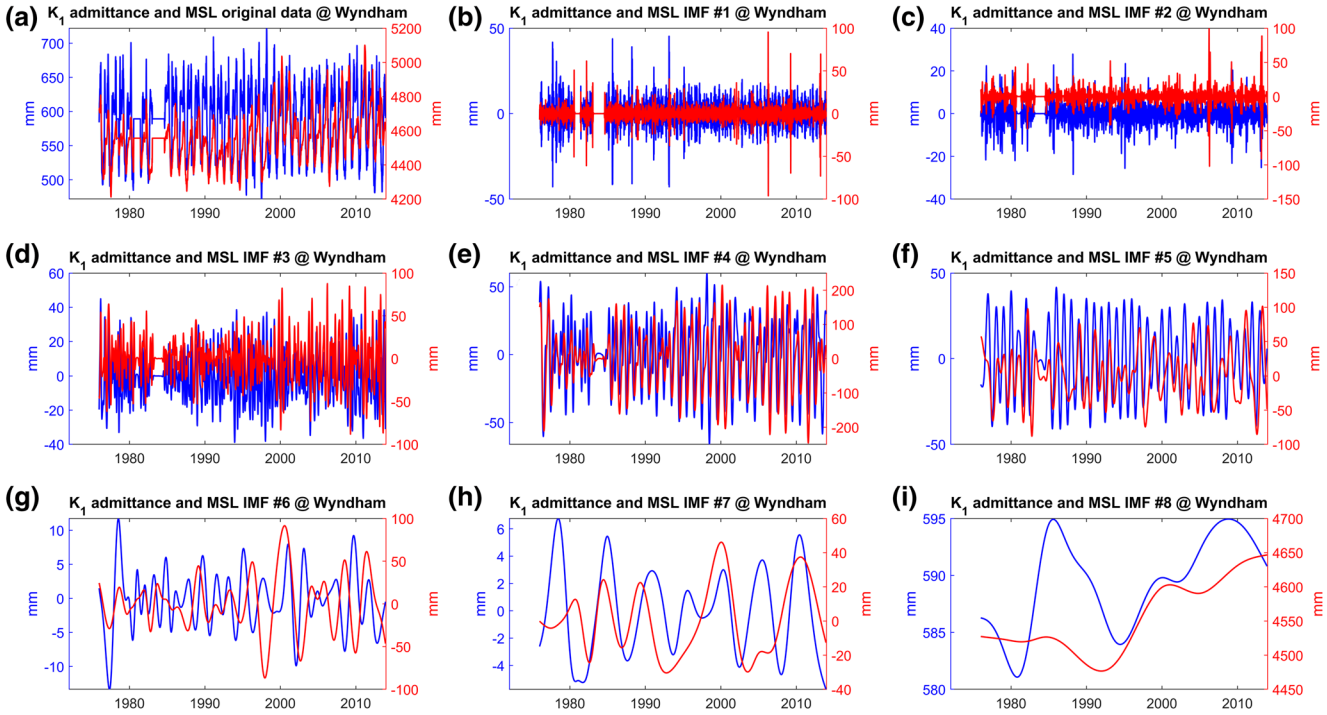

Figure 3. Ensemble empirical mode decomposition comparison between mean sea level (red) and K_1 admittance amplitude (blue) at Wyndham, Australia. The original data is shown in panel (a), and each intrinsic mode functions from 1 to 8 is shown in panels (b) through (i). Units are in millimeter.

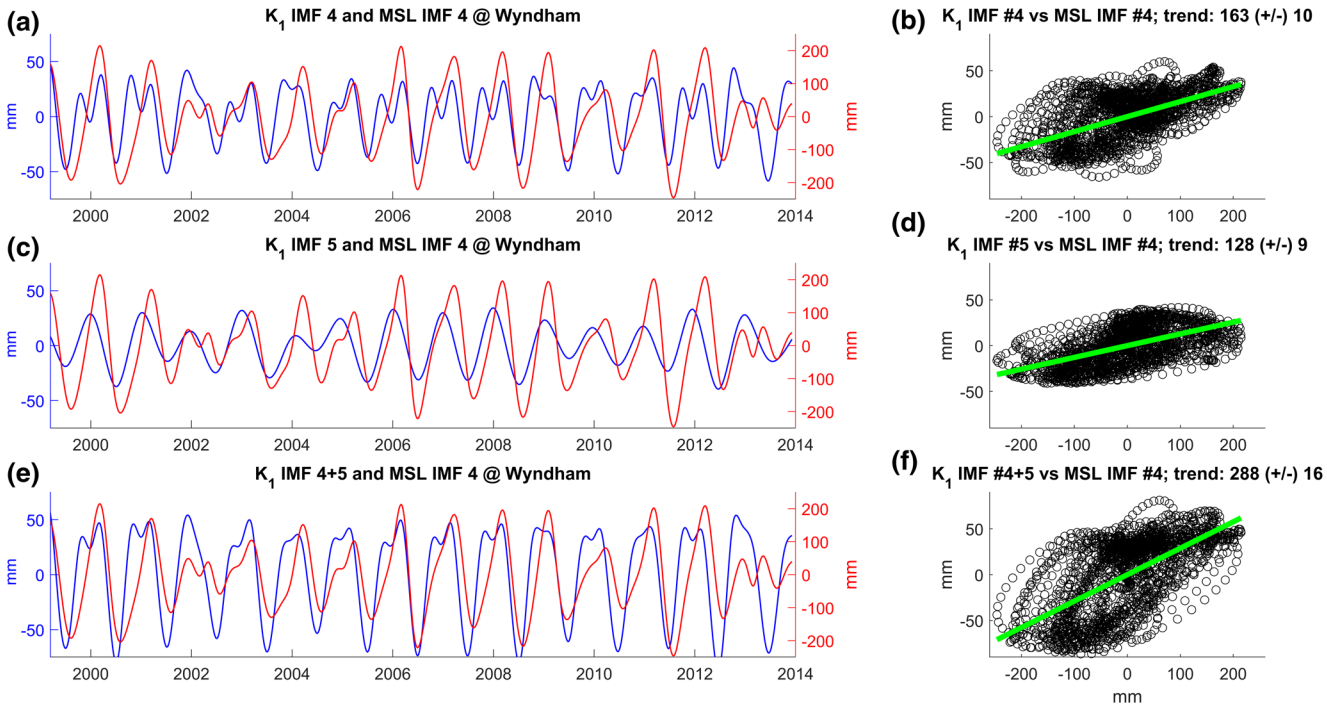

Figure 4. Annual band comparisons between mean sea level (MSL_4) and $K1_4$ (a and b), $K1_5$ (c and d), and $K1_{4+5}$ (e and f) at Wyndham, Australia. Time series (a, c, and e) display a subset of the entire record for ease of visual examination, with vertical units in mm. Scatterplots (b, d, and f) display the detrended K_1 admittance amplitude regressed against MSL. The green lines indicate the robust fit of the regression, with numerical values of the slope and fitting error given in the title, in units of millimeter m^{-1} as the magnitude of the tidal anomaly correlation.

Journal of Geophysical Research: Oceans

10.1029/2020JC016604

Table 2
IMF Comparison Matrix of TACs Between MSL and K_1 Admittance Amplitude at Wyndham, Australia, Showing the Domain of the Sub-Annual (Yellow), Annual (Red), and Inter-Annual (Green) Frequency Bands.

$K_1 \rightarrow$ / MSL ↓	2	23	3	34	4	45	5	56	6	67	7
2	*122.6 ± 18.1 (6.8)*	*211.4 ± 59.8 (3.5)*	84.6 ± 53.4 (1.6)	-	-	-	-	-	-	-	-
3	-	-	*286.9 ± 21.2 (13.6)*	***702.5 ± 50.6 (13.9)***	*432.9 ± 39.6 (10.9)*	-	-	-	-	-	-
4	-	-	-	-	*163.9 ± 10.6 (15.5)*	***288.3 ± 16.5 (17.4)***	*128.3 ± 9.3 (13.8)*	-	-	-	-
5	-	-	-	-	-	-	*182.2 ± 26.0 (7.0)*	***181.9 ± 25.7 (7.1)***	−1.3 ± 4.8 (0.3)	-	-
6	-	-	-	-	-	-	-	-	−11.1 ± 5.3 (2.1)	*16.5 ± 7.6 (2.2)*	*20.5 ± 4.4 (4.6)*

Note. MSL IMFs are on the y-axis, and K1 is on the *x*-axis. Units of TACs and associated errors are in millimetre m^{-1}, and the number in parentheses indicates the signal-to-noise ratio (SNR). Italicized results indicate significance, and bolded results indicate the "best fit" result within each frequency band.

Abbreviations: IMFs, intrinsic mode functions; MSL, mean sea level; TACs, tidal anomaly correlations.

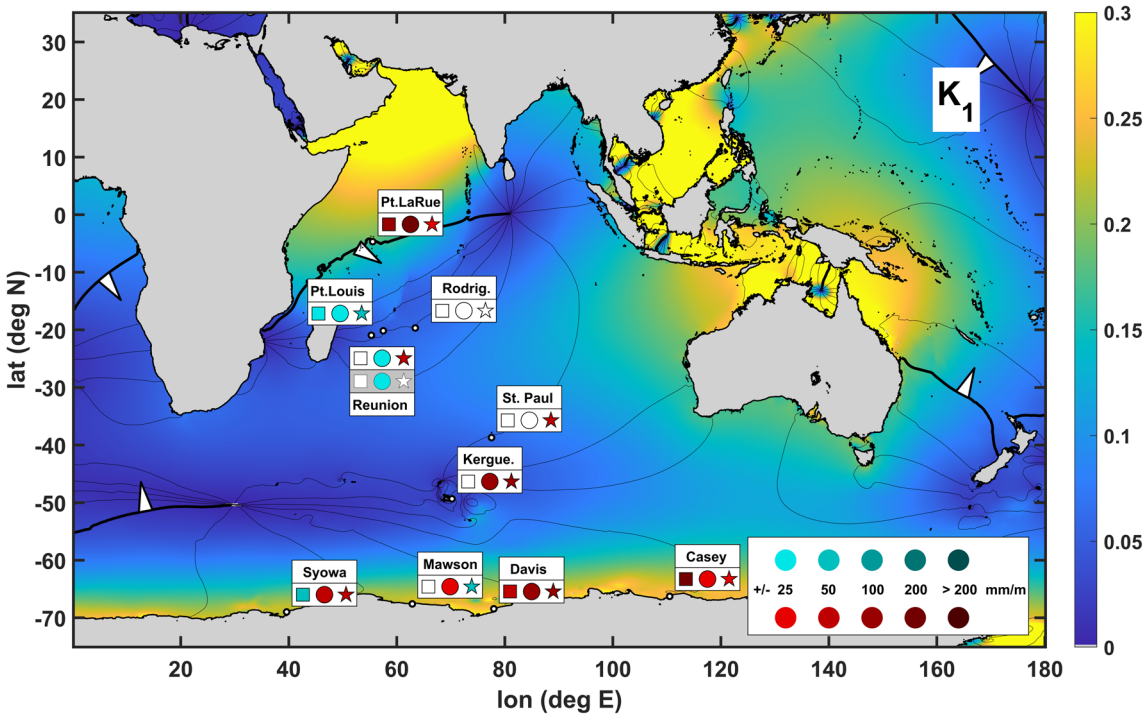

Figure 5. K_1 tidal anomaly correlations (TACs) in the Indian Ocean at open ocean locations and Antarctica. Symbols inside boxes indicate three different frequency bands, squares are the sub-annual (SA) band, circles are the annual (ANN) band, and stars are the interannual (IA) band. Station names are also indicated. Color shading of the symbols indicate positive shades of red) and negative (shades of blue) TACs according to legend at the bottom right. Background colors show tidal amplitudes (corresponding to the color bar at the right in units of meters) and phases (solid lines, in increments of 30°) from the TPXO 7.2 global solution (Egbert & Erofeeva, 2002).

3. Results

We now display the TAC results according to the process above. We will only show maps and tables for the M_2, K_1, and δ-HAT results in the main text; the O_1 and S_2 results will be discussed briefly, and these maps and tables will be provided in the Supporting Information. For each map, we will display the multi-band TACs at each location as a set of shapes (one for each frequency band), with squares for the SA band, circles for the ANN band, and stars for the IA band. We use color shading to indicate the magnitude (shades of red for positive and shades of blue for negative) of the TACs or δ-HATs according to the legend provided in each figure; TACs are charted on a scale of ± 200 mm m^{-1}, and δ-HATs are ± 400 mm m^{-1}. The TACs are only plotted if they are significant (SNR > 2.0) and have a magnitude of ± 10 mm m^{-1}, and δ-HATs are plotted if they are greater than ± 50 mm m^{-1}. The first plot in each set will be of the entire Indian Ocean (same domain as Figure 1), showing the results at open ocean and Antarctic gauges, and the second plot in each set will show each of the four regions, as in Figure 2. For each individual tide, we will also provide a background of the average tidal amplitudes and phases based on the satellite altimeter derived TPXO 7.2 solution (Egbert & Erofeeva, 2002) to provide reference for the average magnitudes of tidal amplitudes. Color scales of the background are indicated by the bar on the right of each figure (units of meter), and solid lines show tidal phases in increments of 30°. For δ-HAT, we will provide only a simple white background.

3.1. Diurnal Results

3.1.1. K_1 Results

The K_1 tidal patterns in the main Indian Ocean (Figure 5) are largely dominated by a large tidal amphidrome south of the Indian subcontinent, and a lesser extended amphidromic feature to the south of Africa. This leads to generally small tidal amplitudes in much of the central Indian basin. Significant amplifica-

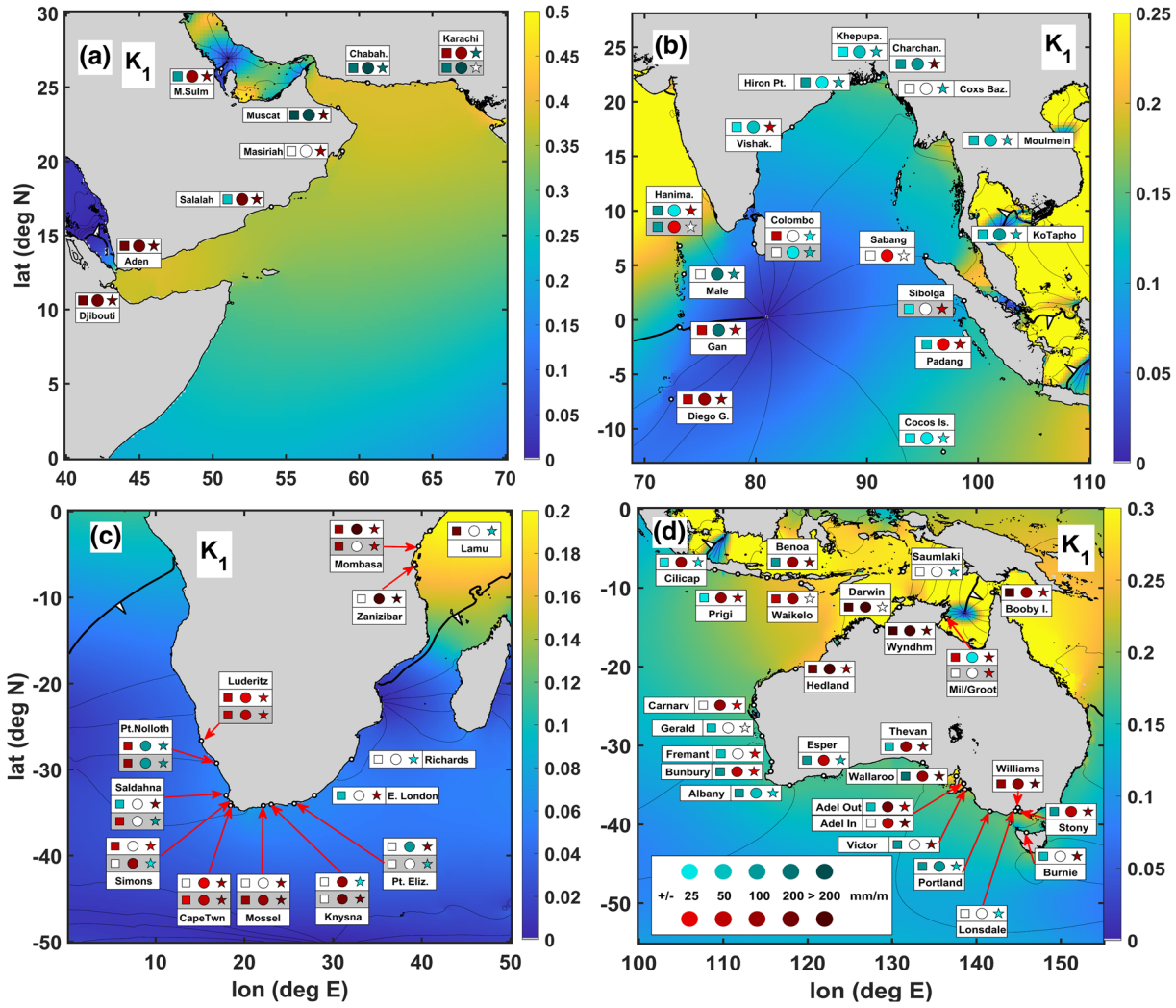

Figure 6. K_1 tidal anomaly correlation (TACs) in four different regions of the Indian Ocean: (a) The Arabian Sea, (b) The Bay of Bengal, (c) Africa, and (d) The Australian region. Symbols inside boxes indicate three different frequency bands, squares are the sub-annual (SA) band, circles are the annual (ANN) band, and stars are the interannual (IA) band. Station names are also indicated. Color shading of the symbols indicate positive shades of red) and negative (shades of blue) TACs according to legend at the bottom right. Background colors show tidal amplitudes (corresponding to the color bar at the right of each subplot in units of meters) and phases (solid lines, in increments of 30°) from the TPXO 7.2 global solution (Egbert & Erofeeva, 2002).

tions in K_1 are found in the Arabian Sea and its connected waters, the northwest shelf of Africa, in Indonesia, and along the Antarctic coast. Most of the Bay of Bengal has small K_1 amplitudes, though some parts of the region have moderate amplitudes. The TACs in the open ocean locations near the amphidromic point in the Seychelles are of generally small negative magnitude or insignificant. An exception to this is seen at Point La Rue, which is near the edge of the amplification region and is strongly positive in all three bands. In Antarctica and at Kergulen Island, results are mostly positive across the spectrum; the only exception to this is Syowa which is mildly negative in the SA band, and Mawson which is slightly negative in the IA band.

In the Arabian Sea and connected regions (Figure 6a), K_1 amplitudes generally increase to the north and to the west with near-constant tidal phases in most places. Within the Persian Gulf is an independent amphidromic structure with a center point just to the north of Bahrain, and amplifications in the northwest and south-central regions of the Gulf. Inside the Red Sea there is a more complex pattern of tidal phases and smaller amplitudes. At the connection of the Red Sea with the Gulf of Aden (the *Bab-el-Mandeb*), we see positive and high magnitude TACs at both tide gauges nearby (Djibouti and Aden). Moving northeast along the coast of the Arabian Peninsula, positive trends in the IA band are also seen at Salalah and Masiriah, but the former has a negative trend in the SA band and the latter is insignificant in the SA and ANN bands.

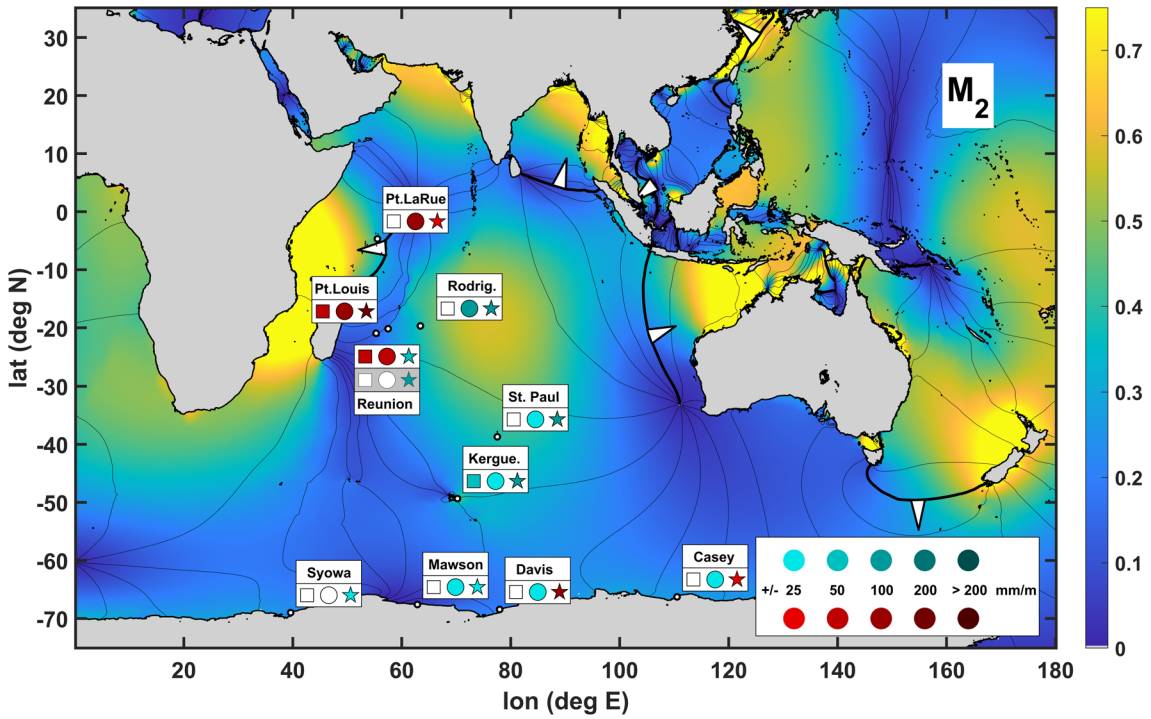

Figure 7. M_2 tidal anomaly correlations in the Indian Ocean at open ocean locations and Antarctica. Symbols and backgrounds are as described in Figure 5.

At Muscat, a positive IA TAC is still seen, but the SA and ANN band show extraordinarily strong negative TACs, which is also seen across the Gulf of Oman at Chabahar, Iran. A strong negative trend is also observed further east at Karachi, Pakistan in the later data set (Karachi-B), though the data from Karachi-A shows a mainly positive trend. Finally, within the Persian Gulf, Mina Sulman has a mixed pattern, with SA being negative, and ANN and IA being positive.

In the Bay of Bengal region (Figure 6b), the Maldives island chain forms a separation between high amplitudes of K_1 found in the Arabian Sea to the west and lower amplitudes seen to the east toward the K_1 amphidrome. This yields a mixed pattern of TACs in and near the Maldives. Male is strongly negative in the ANN and IA bands; Gan is negative in the ANN band but positive in SA and IA. Hanimaadhoo shows a difference between the "A" and "B" records; both show negative TACs in the SA band, but switch from negative to positive in the ANN band. However, nearby Colombo on the island of Sri Lanka is more consistent between its "A" and "B" records (which are separated by 40 years), negative TACs are seen in the IA band in both eras, though the SA band has changed from positive to insignificant, and the ANN band has changed from insignificant to mildly negative. South of the Maldives at Diego Garcia Island and farther away from the amplification region, all three TACs are strongly positive. Within the Bay of Bengal itself, the pattern is much more coherent. Nearly all significant trends are negative in the Bay, including the Andaman Sea. The only exceptions to this are a positive IA TAC at Vishakhapatnam, India and Cox's Bazaar, Bangladesh. The Indonesian gauges to the south of the Bay of Bengal also showed a mixed pattern of mildly negative, mildly positive, and insignificant, with Sibolga showing a temporal change between the "A" and "B" data sets. Finally, Cocos Island far to the south is weakly negative in all bands.

Tides in the African region (Figure 6c) are mainly semidiurnal, so the K_1 amplitudes are small along most of the African coast, with the exception of the area north of the Mozambique channel. The TACs, where significant, are positive at a majority of locations across the spectrum on the Atlantic side along to the bottom of the continent. There are some exceptions, namely, negative ANN and IA bands at Port Nolloth, a negative IA band at Saldahna Bay and Simon's Town in the later ("B") records, and a mildly negative IA band in the "A" record at Knysna. Further north along the Indian Ocean side, TACs are slightly negative or insignificant except for the "A" record of Port Elizabeth and East London. Finally, the far northern locations where

amplitudes are larger show a generally strong positive trend, with only the IA band of Lamu diverging from this pattern as a slight negative.

In Australia (Figure 6d), K_1 is of high amplitude in the northern regions, with complex phase patterns seen in the marginal Indonesian seas and a generally constant-phase tide on the northwest Australian Shelf. There is an isolated amphidromic system seen in the Gulf of Carpentaria. The K_1 tide in the western and southern parts of Australia is of moderate amplitude with a nearly consistent phase, and there are strong amplifications near Adelaide and in the Tasmin Sea. In the northern region, the TACs are mainly positive in the ANN band; only Milner Bay (the "A" data set) and Saumlaki, Indonesia diverge from this pattern, being weakly negative and insignificant, respectively. The SA band is mildly negative in the eastern Indonesia islands, turning consistently positive moving west. The IA band is also nearly always positive, except for one negative at the far northwest (Cilicap, Indonesia), and a few insignificant locations in the northern central part of the map in the Indonesia waters. Three of the northern Australian gauges (Port Hedland, Darwin, and Wyndham) have extremely large positive TACs. Along the western and southern reaches, the SA band is always negative where significant, except for Williamstown. Conversely, the ANN band is nearly always positive where significant; only Albany and Portland show a negative TAC. Finally, the IA band is a bit more mixed, showing positive TACs in most locations, and being negative at two gauges (Albany and Esperance) on the southwest corner of the continent and two gauges on the southeast corner (Portland and Point Lonsdale).

3.1.2. O_1 Results

The O_1 tidal patterns are nearly similar to K_1 (Figure S1) except that there are two major amphidromes in the main Indian basin, one near the southern tip of Sri Lanka, and the other south of Madagascar, and both are connected via the phase lines. However, TACs in the open ocean locations are not as common as for K_1 and are more positive than negative where significant. In the Arabian Sea region O_1 is about half the amplitude of K_1 (Figure S2) with a similar amphidrome. The TACs are generally weak or insignificant, though the IA band is positive at most locations, and the ANN band is negative at almost half of locations. In the Bay of Bengal region (Figure S2b), tidal amplitudes are also about half that of K_1, but the pattern of TACs are fairly coherent; being negative where significant in locations inside the Bay of Bengal, and being positive in the Maldives and most of the Indonesian locations. Diego Garcia is weakly negative across the spectrum.

In Africa (Figure S2c), tidal amplitudes are similar to K_1, small along most the coast, with larger amplitudes north of the Mozambique Channel. The ANN TACs are mostly negative on the Atlantic side and at the tip of the continent, and mainly positive on the Indian side. The IA band is mixed, and the SA TACs in O_1 are nearly always insignificant. Finally, in Australia, the tidal patterns are nearly identical to K_1, with an amphidrome in the Gulf of Carpentaria, and an amplification along the northwest shelf. The SA band is primarily negative in the western Indonesian locations, on the north-central Australian coast, and the southwestern coast, but is positive in the Gulf of Carpentaria and at Adelaide Harbor, and mainly insignificant on the western coast. The ANN band is positive everywhere except on the southwestern coast and at Williamstown where negative TACs are seen, and insignificant on the western coast of Australia and at western Indonesian locations. Finally, the IA band shows mixed results, positive in the Gulf of Carpentaria and near Adelaide, and negative in the north center coast, southwestern coast, and in the Tasman Sea.

For K_1, 56 locations out of 73 were significant in the SA band (77%), of which 22 were positive, 31 were negative, and three were showed a "mixed" behavior between "A" and "B" data sets. For the K_1 ANN band, 58 locations were significant (80%), of which 36 were positive, 20 were negative, and 2 were "mixed." The IA band of K_1 showed 67 locations of significance (89%), with 43 positive, 20 negative, and 4 "mixed." The SA band used the MSL_3 versus $K1_{34}$ IMF combination most often (22 locations), in the ANN band, MSL_4 versus $K1_{45}$ was the dominant choice in more than half of significant locations (36), and in the IA band, the most common IMF combo choice was MSL_5 versus $K1_{56}$ (28). For O_1, there were 33 (45%) significant SA results (12 positive and 21 negative), the ANN band had 24 positive, 17 negative, and 1 mixed (42 total, 58%), and the IA band was significant at 64 locations (85%), with 33 positives, 25 negatives, and 6 mixed. Numerical results for K_1, along with errors, SNRs, and mode combinations chosen are given in Table 3, and O_1 is reported in the Supporting Information (Table S1).

Table 3
Results for K_1 Admittance Amplitude TACs in the Indian Ocean, Separated by Regions of Discussion

	K_1 (SA)			K_1 (ANN)			K_1 (IA)		
Station name	TACs	Error	*IMFs*	TACs	Error	*IMFs*	TACs	Error	*IMFs*
Arabian Sea region									
Djibouti	109.8	42.2	*3vs4*	176.3	17.9	*4vs4*	177.0	20.5	*5vs5*
Aden	141.5	46.1	*3vs4*	149.0	18.8	*4vs45*	117.1	19.3	*5vs56*
Salalah	−31.6	9.7	*3vs3*	152.2	10.0	*4vs45*	157.5	15.1	*5vs56*
Masiriah							83.0	20.1	*6vs6*
Muscat	−231.6	72.8	*3vs34*	−409.5	33.5	*4vs45*	143.5	14.5	*6vs6*
Mina Sulman	−58.4	15.6	*3vs3*	76.2	18.9	*4vs45*	79.4	14.7	*5vs56*
Chabahar	−122.8	50.5	*3vs34*	−347.3	32.6	*4vs45*	−140.7	10.5	*6vs6*
Karachi "A"	94.5	42.7	*2vs3*	91.7	29.7	*4vs45*	−105.5	21.0	6vs6
Karachi "B"	−103.1	50.4	*3vs34*	−226.8	39.2	*4vs45*			
Bay of Bengal region									
Diego Garcia	48.6	7.3	*3vs3*	63.3	7.7	*4vs45*	63.2	3.0	*6vs67*
Gan	47.2	17.1	*3vs34*	−111.9	12.3	*4vs45*	28.1	2.7	*6vs6*
Male				−125.3	6.6	*4vs45*	−87.9	9.3	*5vs56*
Hanimaadhoo "A"	−86.7	26.1	*3vs34*	−17.9	6.5	*4vs45*	37.7	10.4	*6vs6*
Hanimaadhoo "B"	−52.3	23.7	*3vs34*	22.0	6.3	*4vs4*			
Colombo "A"	32.8	13.9	*3vs34*				−23.6	8.2	*5vs6*
Colombo "B"				−12.0	4.2	*4vs45*	−36.8	6.2	*5vs56*
Cocos Island	−18.0	8.4	*3vs4*	−19.1	2.9	*4vs5*	−19.3	7.1	*5vs56*
Hiron Point	−62.1	11.2	*3vs4*	−21.6	1.3	*4vs5*	−48.4	7.4	*6vs67*
Khepupara	−23.3	6.3	*3vs4*	−28.3	2.7	*4vs45*	−26.5	5.3	*6vs7*
Charchanga	−69.7	6.1	*3vs4*	−54.2	5.1	*4vs45*	101.0	11.8	*6vs67*
Coxs Bazaar							−26.9	10.4	*6vs7*
Moulmein	−45.1	5.1	*3vs34*	−26.8	2.5	*4vs45*	−32.7	5.6	*5vs56*
Vishakhapatnam	−13.4	6.5	*3vs4*	−35.9	3.6	*4vs45*	25.9	3.0	*5vs56*
Ko Tapho Noi	−36.2	6.2	*3vs34*	−72.4	6.2	*4vs45*	−36.9	4.7	*5vs56*
Sabang				21.1	4.7	*4vs4*			
Sibolga "A"	21.6	8.6	*2vs2*	−91.0	12.1	*4vs45*			
Sibolga "B"	−16.7	5.4	*3vs3*				26.6	7.7	*5vs5*
Padang	−31.8	6.9	*3vs3*	21.2	7.5	*4vs4*	41.2	7.7	*5vs5*
African region									
Luderitz "A"	34.2	8.5	*3vs34*	11.5	3.8	*4vs45*	11.5	4.7	*5vs56*
Luderitz "B"	39.9	12.1	*3vs34*	30.1	6.7	*4vs45*	40.2	1.0	*6vs7*
Port Nolloth "A"	31.8	14.1	*3vs4*	−63.9	8.6	*4vs5*	−96.5	11.8	*5vs56*
Port Nolloth "B"	68.4	20.2	*3vs34*	−51.2	5.2	*4vs5*	−95.7	31.2	*5vs56*
Saldahna Bay "A"	−31.9	16.7	*2vs23*				97.1	8.6	*5vs5*
Saldahna Bay "B"	26.7	8.7	*3vs3*				−79.6	5.5	*6vs67*
Cape Town "A"	31.7	14.6	*2vs23*				18.5	7.2	*5vs6*
Cape Town "B"				80.1	14.2	*4vs45*	−24.2	3.0	*6vs6*
Simon's Town "A"				24.4	4.7	*4vs5*	58.6	11.2	*5vs56*

Table 3
Continued

	K_1 (SA)			K_1 (ANN)			K_1 (IA)		
Station name	TACs	Error	*IMFs*	TACs	Error	*IMFs*	TACs	Error	*IMFs*
Simon's Town "B"	24.4	7.9	*3vs4*	32.1	8.9	*4vs45*	57.2	9.6	*5vs6*
Mossel Bay "A"							69.6	23.7	*5vs56*
Mossel Bay "B"	60.8	26.0	*3vs34*	82.0	16.1	*4vs5*	102.1	7.2	*6vs7*
Knysna "A"				71.7	20.1	*4vs45*	−13.6	7.2	*5vs6*
Knysna "B"				135.9	32.2	*4vs45*	124.0	17.4	*6vs7*
Port Elizabeth "A"				−97.1	37.1	*4vs45*	56.1	9.1	*5vs6*
Port Elizabeth "B"							−39.2	10.9	*6vs6*
East London	−28.5	14.3	*3vs34*				73.3	18.1	*5vs5*
Richards Bay							−18.4	9.0	*5vs5*
Zanzibar				540.5	43.9	*4vs45*	273.8	24.8	*5vs56*
Mombasa "A"	53.8	12.4	*3vs3*	204.8	37.3	*4vs45*	62.0	12.1	*6vs67*
Mombasa "B"	92.6	18.4	*3vs3*				47.1	7.4	*6vs6*
Lamu	108.6	15.5	*3vs3*				−25.8	3.6	*5vs6*
Australia region									
Cilicap	−22.7	5.6	*3vs3*	58.6	7.1	*4vs45*	−24.3	3.9	*6vs67*
Prigi	−23.3	6.3	*3vs3*	93.2	7.1	*4vs45*	28.5	3.5	*6vs67*
Benoa	−54.2	10.3	*3vs3*	89.2	6.5	*4vs45*	50.5	5.3	*6vs6*
Saumlaki							−32.3	6.1	*5vs56*
Waikelo	38.5	15.1	*2vs2*	54.1	13.6	*4vs4*			
Booby Island	313.9	52.6	*3vs34*	77.8	8.5	*4vs45*	40.4	14.6	*5vs56*
Milner Bay ("A")	41.2	14.2	*3vs34*	−10.3	4.7	*4vs45*	83.3	11.9	*5vs56*
Groote Eylandt ("B")							29.4	5.6	*5vs56*
Darwin	1309.2	168.5	*3vs34*	297.9	24.9	*4vs45*			
Wyndham	702.5	50.6	*3vs34*	288.3	16.5	*4vs45*	181.9	25.7	*5vs56*
Port Hedland	197.8	63.4	*3vs4*	216.8	18.4	*4vs45*	60.4	14.6	*5vs56*
Carnarvon				78.7	17.0	*4vs45*	18.8	8.3	*5vs56*
Geraldton	−42.2	16.9	*3vs4*						
Freemantle	−30.5	12.6	*3vs4*				19.1	3.2	*5vs6*
Bunbury	−66.9	21.4	*3vs34*	32.5	9.1	*4vs5*	15.4	2.2	*6vs7*
Albany	−61.7	14.6	*3vs4*	−37.1	8.7	*4vs45*	−22.0	3.8	*6vs67*
Esperance	−93.3	22.4	*3vs34*	27.1	6.8	*4vs5*	−42.6	15.9	*5vs56*
Thevenard	−38.3	19.2	*3vs4*	80.5	14.8	*4vs5*	52.3	15.4	*5vs56*
Wallaroo	−102.2	31.9	*3vs4*	69.2	21.4	*4vs5*	103.0	21.4	*5vs56*
Port Adelaide (Outer)	−43.6	20.6	*3vs4*	105.4	23.0	*4vs5*	45.6	6.7	*6vs6*
Port Adelaide (Inner)				42.2	13.4	*4vs5*	137.5	22.0	*5vs56*
Victor Harbor	−54.1	18.6	*3vs34*				63.6	16.0	*5vs56*
Portland	−62.9	11.7	*3vs34*	−80.7	7.1	*4vs45*	−36.4	3.4	*6vs7*
Point Lonsdale							−21.5	6.4	*6vs7*
Williamstown	50.2	18.8	*2vs23*	85.2	9.3	*4vs5*	105.3	12.3	*5vs56*
Stony point	−55.1	18.0	*3vs34*	30.7	7.2	*4vs5*	55.2	13.0	*5vs56*
Burnie	−40.8	14.2	*3vs4*				50.8	12.8	*5vs56*

Table 3
Continued

	K_1 (SA)			K_1 (ANN)			K_1 (IA)		
Station name	TACs	Error	*IMFs*	TACs	Error	*IMFs*	TACs	Error	*IMFs*
Indian Ocean Islands									
Port Louis	−15.7	3.1	*3vs3*	−17.0	2.1	*4vs45*	−43.5	3.9	*5vs56*
Rodrigues									
Reunion "A"				−10.0	2.7	*4vs45*	41.2	5.3	*6vs67*
Reunion "B"				−15.5	2.3	*4vs45*			
Point La Rue	62.6	4.9	*3vs34*	130.3	10.7	*4vs45*	21.6	9.6	*5vs56*
St. Paul							26.2	9.7	*5vs56*
Kerguelen				75.2	12.9	*4vs5*	91.8	12.1	*6vs67*
Antarctica									
Syowa Station	−37.9	13.1	*3vs34*	27.0	3.0	*4vs5*	35.1	10.3	*5vs56*
Mawson				19.2	2.9	*4vs5*	−27.9	3.8	*6vs7*
Davis	34.2	16.0	*3vs4*	54.2	6.0	*4vs5*	68.1	17.1	*6vs6*
Casey	100.1	23.0	*3vs34*	20.0	6.0	*4vs5*	21.9	8.0	*5vs5*

Note. Numerical values of the TACs, their associated errors, and the IMFs mode combinations that gave the "best fit" are given for the subannual (SA), annual (ANN), and interannual (IA) frequency bands. IMF mode combinations are listed with the MSL IMF given first. Color shading is used to indicate positive and negative results, and blank entries indicate insignificant results.

Abbreviations: IMFs, intrinsic mode functions; MSL, mean sea level; TACs, tidal anomaly correlations.

3.2. Semidiurnal Results

3.2.1. M_2 Results

The M_2 is tide is generally larger than K_1 in the Indian Ocean, with the exception of Antarctica (Figure 7). There is a clear amphidrome in the Arabian Sea and near the Western coast of Australia, and a weaker amphidrome apparent of the east coast of Madagascar. These points are somewhat connected to each other via the tidal phase lines, and yields coastal amplification regions in the northern parts of the Bay of Bengal (including the Andaman Sea), the northern parts of the Arabian Sea, in the Mozambique Channel along the east coast of Africa, on the northwest Australian Shelf, and in the Tasman Sea. There is also a region of higher amplitudes seen in the center of the Indian basin between the amphidromic points. The TACs in the western Seychelles and at Point La Rue to the north are positive in the ANN band, but are negative to the east and south. The IA band is more consistently negative in the central part of the basin, though Port Louis and Point La Rue are positive. Antarctica has mainly insignificant or weakly negative TACs in the ANN and IA bands, as semidiurnal amplitudes are small here. The SA band is insignificant at most locations.

In the Arabian Sea region (Figure 8a), the influence of the amphidromic point yields larger amplitudes in the southern and northern parts of this sub-region, and lesser amplitudes in the center. Within the Persian Gulf, two small amphidromic points are apparent in the northwest and southern parts, and a small amplification of M_2 is seen in the Gulf of Aden. The M_2 TACs are generally smaller and less significant than K_1. The SA band is negative where significant, except at Aden. The ANN band is also negative where significant, except for Aden and the early Karachi record. The IA band has a mixed pattern; negative at Djibouti, in the Persian Gulf at Mina Sulman, and at Karachi in the later record, but strongly positive at locations on the Gulf of Oman.

In the Bay of Bengal region (Figure 8b), the largest amplitudes are found in the northern parts of the Bay, in the Andaman Sea, and in the southwest part of the domain. The M_2 TACs in the Maldives and at the Indonesian locations are positive at most locations at all bands, with the exception of Gan, which is negative

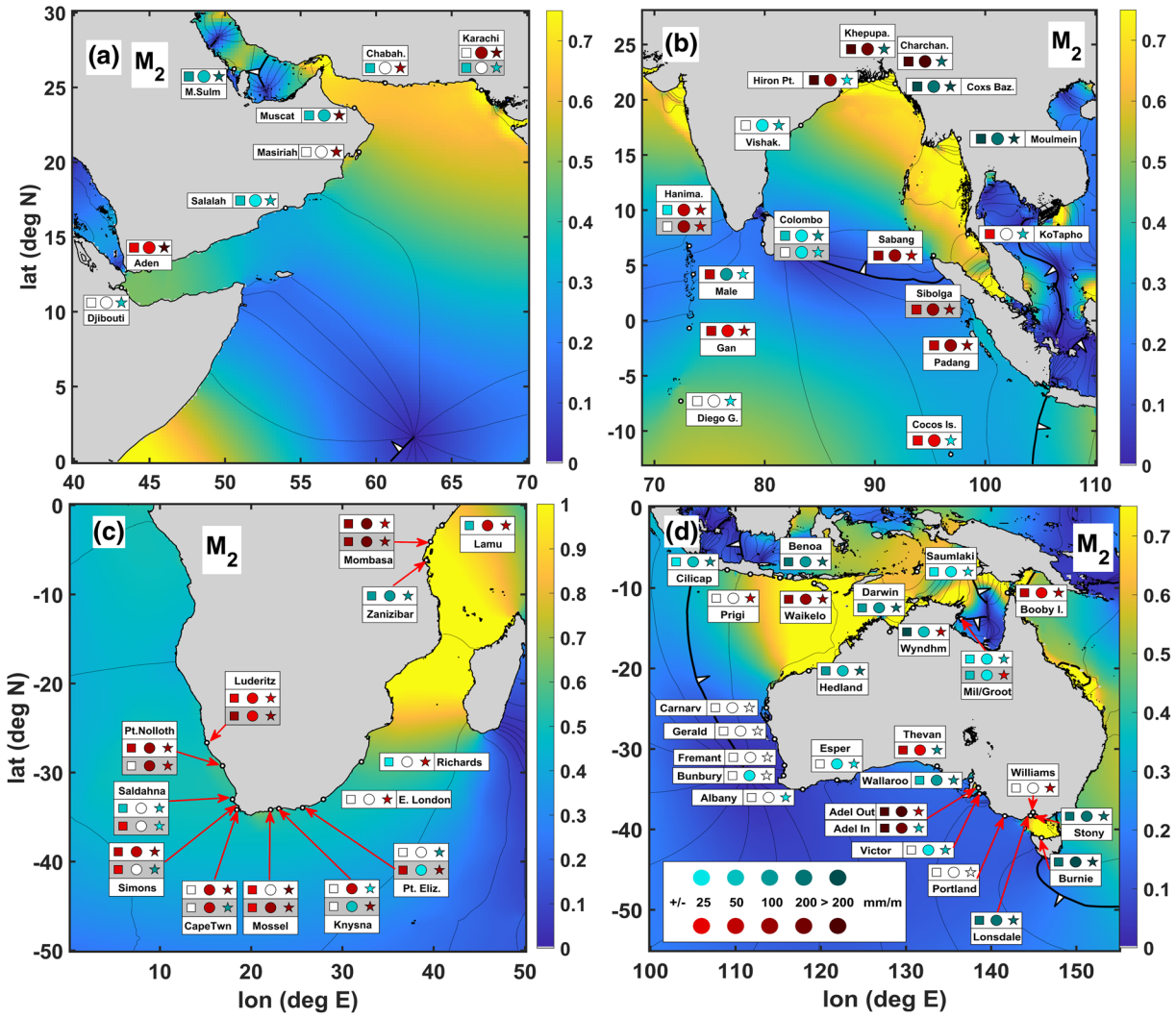

Figure 8. M_2 tidal anomaly correlations in four different regions of the Indian Ocean: (a) The Arabian Sea, (b) The Bay of Bengal, (c) Africa, and (d) The Australian region. Symbols and backgrounds are as described in Figure 6.

for ANN and IA, and the early record of Hanimaadhoo which is negative in SA. However, Colombo in Sri Lanka is coherently negative for nearly all determinations. Within the Bay of Bengal, all IA TACs are negative, and half the ANN TACs are negative, but there is a concentration of strongly positive TACs in the SA and ANN band concentrated in Bangladesh near the Ganges River Delta, though the ANN band at Cox's Bazaar is strongly negative.

The M_2 tidal amplitudes are much larger than K_1 in the majority of the African sub-region, with a large amplification in the Mozambique channel (Figure 8c). The ANN TACs are predominantly positive except for weak negatives seen at the southern tip (Knysna and Port Elizabeth), and at Zanzibar in the north. The SA band is also predominantly positive where significant, except for Zanzibar and Lamu. The IA band is mostly positive, except for Cape Town, and Zanzibar. The "A" and "B" data records are more consistent than for K_1, as the later data mirrors the early data more consistently. The only exceptions are seen in the IA band at a few southern locations.

The M_2 TACs in the Australian region are presented in Figure 8d. Tidal amplitudes are largest in the northern parts of the continent, especially on the northwestern shelf, and like K_1, a complex pattern is found inside the marginal Indonesian Seas. Unlike K_1, however, there is no amphidrome inside the Gulf of Carpentaria, and amplitudes are small in the center of the Gulf, but quite large at the eastern and western

boundaries. There is also a large amplification in M_2 in the Tasman Sea. The SA and ANN TACs are negative at most locations, with the exception of Booby Island in the Torres Strait at the eastern entrance to the Gulf of Carpentaria, at Waikelo, Indonesia, and in Adelaide Harbor. The negative TACs are extraordinarily strong in the Tasman Sea, but are insignificant at Williamstown itself (which is inside a sheltered harbor). The IA band is negative at a majority of locations but is positive in the Gulf of Carpentaria, at a few Indonesian locations (Waikelo and Prigi), and at Williamstown. Finally, nearly all TACs on the western coast are insignificant, as the presence of the amphidromic point there makes the tidal amplitudes extremely small.

3.2.2. S_2 Results

The tidal patterns of S_2 are similar to M_2 (Figure S3). The TAC patterns in the open ocean are also similar to M_2, except that there are more positive trends seen. Antarctic TACs are mixed, but more often significant than M_2. In the Arabian Sea region (Figure S4a), the TACs are more coherent than M_2. The SA band is always negative, the ANN band is consistently negative in the Gulf of Aden and consistently positive in the Gulf of Oman and Persian Gulf, and the IA band is mixed. In the Bay of Bengal region (Figure S4b), TACs are mainly positive at Indonesian locations and in the north part of the Bay in Bangladesh, except at Cox's Bazaar, which is always negative. The locations in the Andaman Sea are also negative, as is Colombo in Sri Lanka, while the Maldives show a mixed and mainly insignificant TAC pattern.

In Africa (Figure S4c), the TAC patterns are approximately opposed to M_2 in the ANN band, as the Atlantic side shows a generally negative trend while the Indian side and the southern tip of the continent generally have positive trends. The SA band is mostly insignificant in South Africa, except north of the Mozambique Channel, where it is consistently negative. The IA band shows a notable temporal shift; the majority of the "A" records are negative, and the majority of the "B" records are positive. Finally, in Australia (Figure S4d), we see a high-amplitude region in the northwest shelf, a complicated distribution in the Indonesian Seas, and a low-amplitude region in the center of the Gulf of Carpentaria. However, the Tasman Sea does not show such a strong amplification for S_2 as was seen in M_2, though there is a different region of amplification in the southern central part of the Australian coast near Thevanard. The SA band TACs are mainly negative, with the exception of Wyndham and Darwin, at both Adelaide gauges, and in the Tasman Sea. A similar pattern is seen for the ANN band, mostly negative except for Adelaide and most Tasman Sea locations. The IA band, where significant, is negative in most northern locations and positive in most southern locations. The western coast, similar to M_2, is extremely near the amphidromic point, so TACs are generally insignificant here, and are negative where significant.

For the M_2 TACs, the SA band had a total of 50 significant locations (69%), 25 positive, 24 negative, and 1 "mixed." In the ANN band, 25 locations were positive, 31 were negative, and 1 was "mixed," for a total of 57 (78%). In the IA band, we find 68 total significant locations (90%), with 26 positives, 36 negatives, and 6 "mixed" results. The IMF of the SA band revealed that MSL_3 versus $M2_{34}$ was the most common (25), in the ANN band, MSL_4 versus $M2_{45}$ was the most common (38), and in the IA band, MSL_5 versus $M2_{56}$ was the most often seen (18). For the SA band of S_2, 56 (77%) of locations were significant (22 positives, 34 negatives), the ANN band of S_2 showed 57 significant results (79%), with 21 positives, 32 negatives, and 4 mixed results, and the IA band of S_2 showed significance at 66 locations (87%), including 27 positives, 31 negatives, and 8 mixed results. Numerical results for M_2, along with errors, SNRs, and mode combinations chosen are given in Table 4, and the S_2 results are given in the Supporting Information (Table S2).

3.3. δ-HAT Results

Finally, we display the results of the combined tidal variability expressed by the δ-HAT. No tidal solution backgrounds are provided here, as the δ-HAT represents a combination of tidal amplitudes, and a simple addition of the tidal amplitude maps would not be meaningful. In Figure 9, we see that Point La Rue and the early record of Reunion are consistently positive, though the Reunion "B" record is fully insignificant. Nearby Rodrigues Island is weakly negative across the spectrum. Other locations are either weakly mixed, or insignificant.

In Figure 10a, the Arabian Sea δ-HATs are shown. The SA band is always negative, while the ANN band is positive in the Gulf of Aden and the Persian Gulf and negative in the Gulf of Oman. The IA band is positive in the Gulf of Aden, and negative in the Persian Gulf and Gulf of Oman. In the Bay of Bengal region (Figure 10b), we see a consistently positive TAC spectrum at Indonesian locations, and a consistently negative

Table 4
Results for M_2 Admittance Amplitude TACs in the Indian Ocean, Separated by Regions of Discussion

	M_2 (SA)			M_2 (ANN)			M_2 (IA)		
Station name	TACs	Error	*IMFs*	TACs	Error	*IMFs*	TACs	Error	*IMFs*
Arabian Sea region									
Djibouti							−35.9	7.3	*5vs6*
Aden	11.9	4.6	*3vs4*	14.9	2.3	*4vs45*	220.8	17.6	*6vs67*
Salalah	−29.6	4.9	*3vs4*	−14.5	3.4	*4vs4*	−34.9	15.5	*6vs6*
Masiriah							56.0	16.9	*5vs5*
Muscat	−47.3	17.6	*3vs34*	−43.3	11.8	*4vs45*	144.2	7.3	*6vs67*
Mina Sulman	−79.5	20.7	*3vs34*	−26.1	8.6	*4vs45*	−106.0	9.3	*6vs67*
Chabahar	−44.5	11.0	*3vs34*				64.9	6.8	*6vs67*
Karachi “A”				73.0	14.6	*4vs4*	197.4	41.6	*6vs6*
Karachi “B”	−36.3	14.3	*3vs34*				−30.0	7.5	*6vs6*
Bay of Bengal region									
Diego Garcia							−12.8	4.5	6vs6
Gan	38.6	9.3	*3vs3*	12.7	3.0	*4vs5*	27.7	7.8	*5vs56*
Male	29.9	13.3	*3vs34*	−53.0	8.1	*4vs45*	−11.0	2.5	*6vs7*
Hanimaadhoo “A”	−18.8	8.3	*3vs3*	26.1	7.7	*4vs45*	32.4	15.9	*5vs56*
Hanimaadhoo “B”				60.1	5.5	*4vs45*	49.2	14.9	*5vs56*
Colombo “A”	−30.7	7.6	*3vs34*	−11.2	1.3	*4vs5*	−64.7	5.9	*6vs6*
Colombo “B”				−10.9	1.5	*4vs5*	−12.1	4.4	*5vs56*
Cocos Island	10.8	4.6	*3vs4*	12.3	2.4	*4vs45*	−17.5	2.5	*5vs6*
Hiron Point	241.7	30.9	*3vs34*	95.5	4.6	*4vs45*	−17.4	3.8	*5vs6*
Khepupara	361.4	44.2	*3vs34*	189.6	9.1	*4vs45*	−192.3	52.6	*6vs67*
Charchanga	369.0	28.1	*3vs34*	207.2	11.7	*4vs45*	−134.1	32.7	*6vs6*
Coxs Bazaar	−260.3	37.1	*3vs4*	−142.7	13.7	*4vs45*	−298.4	16.8	*6vs6*
Moulmein	−274.6	22.2	*3vs34*	−141.4	8.1	*4vs45*	−235.5	46.2	*6vs6*
Vishakhapatnam				−10.6	4.0	*4vs45*	−40.7	3.7	*6vs6*
Ko Tapho Noi	18.5	7.2	*2vs2*				−34.4	3.8	*6vs6*
Sabang	68.6	10.3	*3vs3*	61.8	16.8	*4vs45*	43.8	14.4	*5vs5*
Sibolga “A”	25.1	12.2	*3vs34*	96.4	11.9	*4vs45*	99.0	5.5	*5vs56*
Sibolga “B”	43.1	8.3	*3vs34*	73.7	11.7	*4vs45*	93.8	8.9	*5vs56*
Padang	27.7	4.2	*3vs3*	58.1	9.3	*4vs45*	88.7	7.0	*5vs56*
African region									
Luderitz “A”	16.1	7.3	*3vs34*	13.1	3.8	*4vs45*	17.3	6.2	*6vs7*
Luderitz “B”	56.0	13.2	*3vs34*	12.2	5.8	*4vs4*	71.2	8.7	*5vs5*
Port Nolloth “A”	30.7	11.2	*3vs4*	90.6	11.4	*4vs45*	93.7	12.0	*6vs67*
Port Nolloth “B”				51.0	8.0	*4vs45*	48.4	9.4	*5vs6*
Saldahna Bay “A”	−39.8	15.7	*3vs34*				−33.4	8.5	*6vs7*
Saldahna Bay “B”	10.5	3.5	*3vs4*				−24.9	3.8	*6vs7*
Cape Town “A”	25.9	10.7	*3vs34*	46.5	6.9	*4vs45*	74.7	12.5	*6vs67*
Cape Town “B”	22.0	5.1	*3vs3*				−85.8	6.5	*6vs67*
Simon's Town “A”				45.5	3.4	*4vs5*	79.9	7.8	*5vs5*

Table 4
Continued

	M_2 (SA)			M_2 (ANN)			M_2 (IA)		
Station name	TACs	Error	*IMFs*	TACs	Error	*IMFs*	TACs	Error	*IMFs*
Simon's Town "B"				30.4	7.9	*4vs45*	−65.6	15.4	*6vs67*
Mossel Bay "A"	22.7	8.3	*3vs3*				108.9	20.6	*5vs56*
Mossel Bay "B"	21.0	6.9	*3vs3*	54.2	13.0	*4vs45*	79.0	7.7	*6vs67*
Knysna "A"				49.0	10.9	*4vs45*	−16.7	5.3	*6vs6*
Knysna "B"				−30.3	7.1	*4vs5*	68.1	25.0	*5vs56*
Port Elizabeth "A"							−92.3	12.0	*6vs6*
Port Elizabeth "B"	30.6	7.4	*3vs34*	−12.3	3.6	*4vs5*	53.1	5.5	*6vs7*
East London							41.0	3.5	*6vs7*
Richards Bay	−15.8	7.4	*3vs34*				30.7	6.7	*5vs6*
Zanzibar	−94.5	10.3	*3vs4*	−81.9	13.0	*4vs45*	−58.4	7.6	*6vs67*
Mombasa "A"	52.8	14.4	*3vs34*	144.5	20.8	*4vs45*	26.2	3.9	*6vs7*
Mombasa "B"	68.3	20.3	*2vs2*	116.5	20.1	*4vs5*	98.6	5.9	*6vs67*
Lamu	−30.5	12.3	*3vs4*	47.4	7.5	*4vs5*	36.1	7.2	*6vs6*
Australia region									
Cilicap	−22.8	3.4	*3vs4*	−32.0	2.5	*4vs45*	−50.2	3.6	*5vs56*
Prigi							45.4	3.4	*6vs67*
Benoa	−103.1	19.2	*2vs23*	−90.8	4.6	*4vs4*	−154.2	18.1	*5vs56*
Saumlaki	−13.1	5.8	*3vs4*	−17.5	5.4	*4vs45*	−19.1	8.6	*6vs6*
Waikelo	87.3	29.4	*3vs34*	82.7	20.2	*4vs45*	89.6	13.3	*5vs56*
Booby Island	33.1	5.1	*3vs34*	14.7	2.4	*4vs45*	32.4	3.9	*6vs7*
Milner Bay ("A")	−13.7	2.0	*3vs4*	−20.1	1.8	*4vs45*	−34.6	4.2	*6vs6*
Groote Eylandt ("B")	−28.2	3.4	*3vs4*	−18.1	1.2	*4vs45*	16.3	3.9	*6vs67*
Darwin	−98.2	38.4	*3vs34*	−72.2	3.0	*4vs5*	−146.2	15.2	*5vs56*
Wyndham	−547.5	63.5	*3vs34*	−29.8	13.6	*4vs45*	46.1	6.2	*6vs7*
Port Hedland	−86.3	17.0	*3vs4*	−42.5	3.3	*4vs5*	−104.0	13.0	*5vs56*
Carnarvon									
Geraldton									
Freemantle									
Bunbury				−10.3	1.5	*4vs45*			
Albany							−14.7	1.9	*6vs67*
Esperance				−14.0	1.4	*4vs5*	−19.2	1.8	*6vs67*
Thevenard	39.6	13.2	*3vs34*	12.7	5.8	*4vs4*	−52.9	5.3	*6vs67*
Wallaroo	−49.5	13.1	*3vs34*	−50.2	3.4	*4vs5*	−75.5	4.6	*5vs5*
Port Adelaide (Outer)	256.2	84.0	*3vs34*	213.9	17.7	*4vs45*	37.0	5.7	*5vs5*
Port Adelaide (Inner)	350.5	76.6	*3vs34*	139.0	15.1	*4vs45*	−30.2	11.1	*6vs67*
Victor Harbor				−20.2	2.1	*4vs5*	−36.8	3.1	*5vs56*
Portland									
Point Lonsdale	−113.3	11.3	*3vs34*	−174.5	8.7	*4vs45*	−155.9	10.1	*5vs56*
Williamstown							49.1	4.7	*6vs67*
Stony Point	−131.0	17.2	*3vs34*	−135.8	7.3	*4vs5*	−149.0	15.5	*5vs56*

Table 4
Continued

Station name	M_2 (SA) TACs	Error	*IMFs*	M_2 (ANN) TACs	Error	*IMFs*	M_2 (IA) TACs	Error	*IMFs*
Burnie	**−190.4**	**35.3**	*3vs34*	**−457.3**	**30.6**	*4vs45*	**−227.0**	**32.0**	*5vs56*
Indian Ocean Islands									
Port Louis	**42.8**	**7.2**	*3vs3*	**51.3**	**5.8**	*4vs45*	**154.1**	**11.0**	*5vs56*
Rodrigues				**−69.1**	**7.8**	*4vs45*	**−89.2**	**12.1**	*5vs56*
Reunion "A"	**25.9**	**12.3**	*3vs3*	**34.1**	**8.8**	*4vs45*	**−31.8**	**13.0**	*5vs6*
Reunion "B"							**−50.6**	**3.0**	*6vs6*
Point La Rue				**68.0**	**4.7**	*4vs45*	**20.0**	**1.9**	*5vs6*
St. Paul				**−24.7**	**5.8**	*4vs45*	**−88.4**	**11.5**	*5vs56*
Kerguelen	**−39.9**	**9.6**	*3vs4*	**−20.3**	**11.0**	*4vs4*	**−86.0**	**20.9**	*5vs6*
Antarctica									
Syowa Station							**−10.2**	**3.6**	*5vs56*
Mawson				**−13.8**	**1.8**	*4vs5*	**−17.2**	**5.1**	*6vs67*
Davis				**−14.8**	**2.3**	*4vs5*	**69.0**	**10.1**	*6vs67*
Casey				**−12.1**	**4.1**	*4vs4*	**20.7**	**8.3**	*6vs67*

Note. Numerical values of the TACs, their associated errors, and the IMFs mode combinations that gave the "best fit" are given for the sub-annual (SA), annual (ANN), and interannual (IA) frequency bands. IMF mode combinations are listed with the MSL IMF given first. Color shading is used to indicate positive and negative results, and blank entries indicate insignificant results.

Abbreviations: IMFs, intrinsic mode functions; MSL, mean sea level; TACs, tidal anomaly correlations.

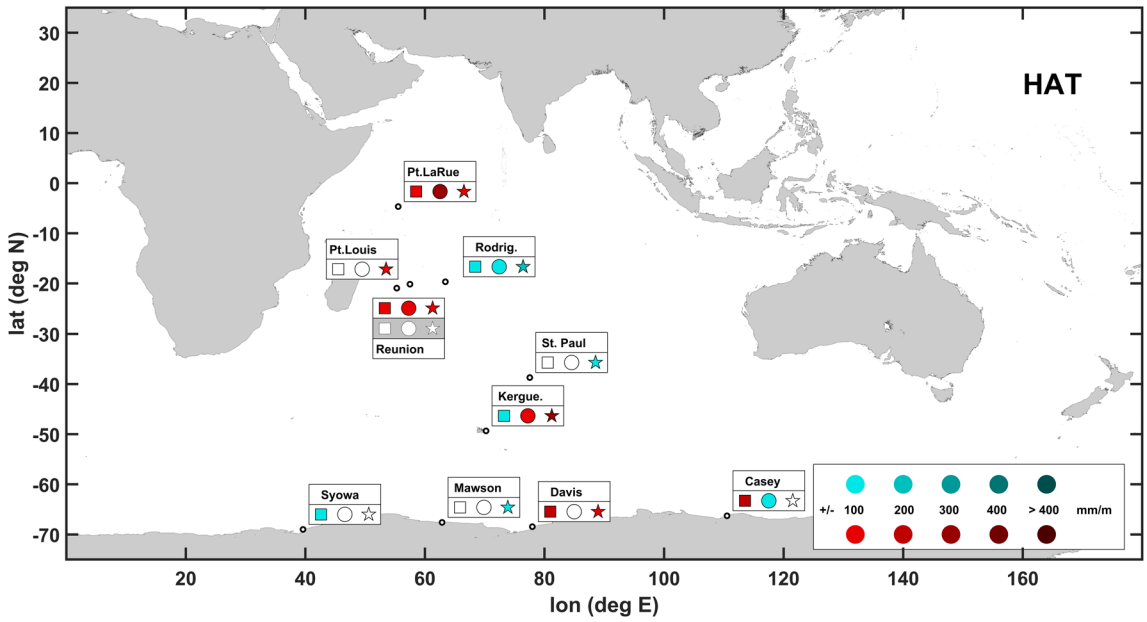

Figure 9. δ-highest astronomical tide in the Indian Ocean, showing open ocean locations and Antarctica. Symbols inside boxes indicate three different frequency bands, squares are the sub-annual (SA) band, circles are the annual (ANN) band, and stars are the interannual (IA) band. Station names are also indicated. Color shading of the symbols indicate positive shades of red) and negative (shades of blue) tidal anomaly correlations according to legend at the bottom right.

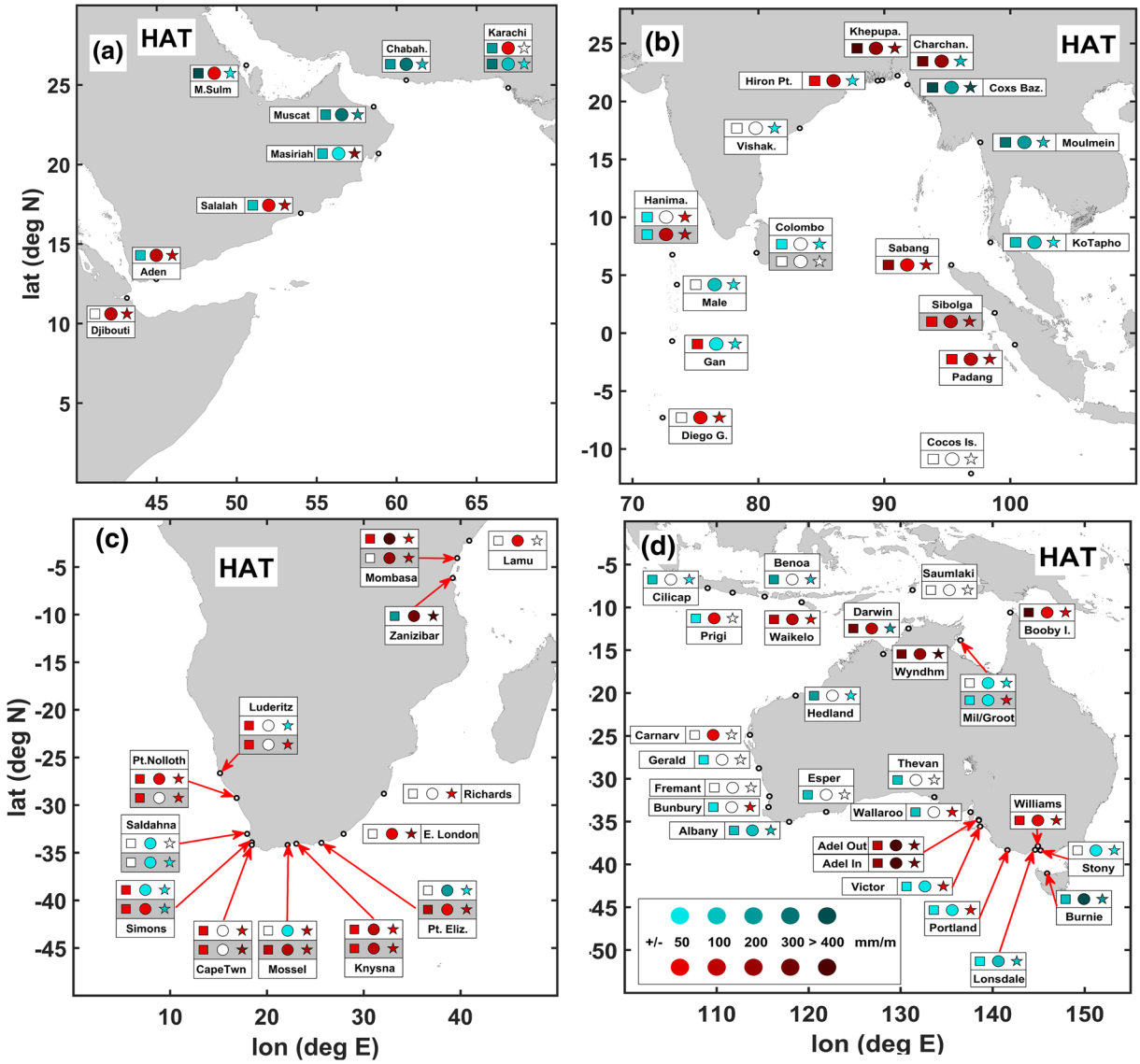

Figure 10. δ-highest astronomical tide in four different regions of the Indian Ocean: (a) The Arabian Sea, (b) The Bay of Bengal, (c) Africa, and (d) The Australian region. Symbols inside boxes indicate three different frequency bands, squares are the sub-annual (SA) band, circles are the annual (ANN) band, and stars are the interannual (IA) band. Station names are also indicated. Color shading of the symbols indicate positive (shades of red) and negative (shades of blue) tidal anomaly correlation according to legend at the bottom right.

TAC spectrum in the Andaman Sea. The SA and ANN bands at the Bangladesh gauges near the Ganges River Delta (except for Cox's Bazaar) are strongly positive, but the IA band is almost always negative. Results in the Maldives and nearby islands are mixed. The ANN band is negative at Gan and Male and positive elsewhere else nearby. The δ-HATs in Africa (Figure 10c) are predominantly positive in all frequency bands, particularly in the later ("B") records. The only exceptions to this are at Saldahna Bay (ANN and IA), at Simon's Town (IA), and at Zanzibar (SA). The majority of the δ-HATs in Australia are slightly negative or insignificant (Figure 10d). However, there are some strong exceptions to this. In the Torres Strait at Booby Island, and in the northern central part of the domain (especially at Wyndham and Darwin), extraordinarily strong positive δ-HATs are found. Other locations where extremely strong positive δ-HATs can be found are within harbors, namely, both Adelaide tide gauges, and at Williamstown.

Summarizing the δ-HAT results, we see 26 positive and 31 negative results (total of 57%, 78%) in the SA band. The ANN band had 52 significant locations (71%), with 30 positives, 18 negatives, and 4 "mixed." The IA band of δ-HAT revealed 33 positive, 26 negative, and 3 mixed results, for a total of 62 (82%). The "best fit"

Table 5
Results for δ-HATs in the Indian Ocean, Separated by Regions of Discussion

	δ-HAT (SA)			δ-HAT (ANN)			δ-HAT (IA)		
Station name	TACs	Error	IMFs	TACs	Error	IMFs	TACs	Error	IMFs
Arabian Sea region									
Djibouti				124.0	18.2	4vs45	141.9	64.4	6vs6
Aden	−151.4	34.5	3vs3	122.9	17.4	4vs45	192.4	31.7	6vs6
Salalah	−175.9	21.8	3vs34	83.5	13.3	4vs45	168.2	27.8	5vs56
Masiriah	−140.4	70.2	3vs34	−67.2	29.2	4vs5	231.1	57.6	6vs6
Muscat	−286.8	82.3	3vs34	−358.9	38.6	4vs45	−244.6	50.3	5vs56
Mina Sulman	−416.1	54.5	3vs3	55.2	11.6	4vs5	−65.2	16.7	6vs7
Chabahar	−217.6	49.8	3vs34	−324.2	40.2	4vs45	−165.1	48.4	5vs56
Karachi "A"	−282.1	101.0	3vs34	87.6	23.5	4vs5			
Karachi "B"	−337.4	58.1	3vs34	−159.7	42.1	4vs45	−67.7	10.5	6vs6
Bay of Bengal region									
Diego Garcia				52.3	8.1	4vs45	63.0	7.0	6vs67
Gan	75.7	14.5	3vs3	−50.0	16.1	4vs45	−75.6	22.6	5vs5
				−177.4	14.8	4vs45	−64.6	22.4	5vs56
Hanimaadhoo "A"	−83.4	20.1	3vs3				91.3	25.1	5vs56
Hanimaadhoo "B"	−62.1	25.0	3vs3	104.7	13.9	4vs45	106.1	30.3	5vs56
Colombo "A"	−99.6	34.5	2vs23				−85.1	26.5	5vs56
Colombo "B"									
Cocos Island									
Hiron Point	98.5	42.9	3vs34	100.3	7.9	4vs45	−61.8	25.9	5vs56
Khepupara	551.0	61.6	3vs34	285.0	14.9	4vs45	236.9	63.2	5vs56
Charchanga	307.4	39.7	3vs34	224.0	21.1	4vs45	−165.1	46.4	6vs67
Coxs Bazaar	−520.6	74.7	3vs34	−264.8	24.4	4vs45	−420.8	35.6	6vs6
Moulmein	−371.0	31.3	3vs34	−214.8	12.4	4vs45	−149.8	16.2	5vs56
Vishakhapatnam							−66.3	3.5	6vs6
Ko Tapho Noi	−151.2	11.7	3vs4	−114.8	10.0	4vs45	−56.2	6.7	6vs6
Sabang	251.2	40.2	2vs2	79.2	21.2	4vs4	173.0	24.1	5vs5
Sibolga "A"	63.3	23.3	2vs2	81.3	14.0	4vs5	165.8	8.5	5vs56
Sibolga "B"	62.8	22.3	2vs2	143.9	26.9	4vs45	154.2	15.5	5vs56
Padang	70.8	22.0	2vs2	156.1	42.7	4vs45	189.6	23.9	5vs56
African region									
Luderitz "A"	94.6	20.4	3vs34				−88.5	8.5	6vs6
Luderitz "B"	69.1	17.3	3vs3				54.5	1.0	6vs7
Port Nolloth "A"	76.9	24.0	3vs3	72.2	19.4	4vs4	89.1	9.3	6vs7
Port Nolloth "B"	88.0	37.6	3vs34				74.1	14.3	5vs6
Saldahna Bay "A"				−65.2	26.2	4vs45			
Saldahna Bay "B"				−58.0	12.3	4vs4	−76.0	7.6	6vs6
Cape Town "A"	68.9	28.3	3vs34	−52.1	19.9	4vs45	−89.5	17.9	5vs56
Cape Town "B"	78.9	22.2	3vs3	59.4	21.5	4vs4	−161.1	13.4	6vs67
Simon's Town "A"	92.9	35.3	3vs34				64.5	11.5	6vs6

Table 5
Continued

Station name	δ-HAT (SA) TACs	δ-HAT (SA) Error	δ-HAT (SA) IMFs	δ-HAT (ANN) TACs	δ-HAT (ANN) Error	δ-HAT (ANN) IMFs	δ-HAT (IA) TACs	δ-HAT (IA) Error	δ-HAT (IA) IMFs
Simon's Town "B"	63.9	31.2	3vs34				222.9	40.6	5vs56
Mossel Bay "A"				−61.2	29.6	4vs5	184.5	35.7	5vs6
Mossel Bay "B"	103.3	47.8	3vs34	133.2	25.8	4vs5	127.0	10.3	6vs7
Knysna "A"	52.5	18.3	3vs4	157.2	29.1	4vs45	76.1	14.9	6vs7
Knysna "B"	89.1	39.8	3vs34	165.6	38.0	4vs45	175.4	32.9	6vs6
Port Elizabeth "A"				−210.2	51.6	4vs45	−80.4	28.7	6vs7
Port Elizabeth "B"	127.7	29.9	3vs34	77.6	23.4	4vs5	127.8	42.0	5vs56
East London				51.0	24.3	4vs45	262.4	30.9	5vs56
Richards Bay							52.0	9.7	5vs6
Zanzibar	−284.9	66.6	3vs34	350.3	30.2	4vs5	491.3	41.9	5vs56
Mombasa "A"	78.4	34.4	3vs34	429.1	46.6	4vs45	58.3	12.2	6vs7
Mombasa "B"				258.7	49.1	4vs4	139.4	18.0	6vs6
Lamu				83.4	34.9	4vs4			
Australia region									
Cilicap	−141.5	13.8	3vs34				−95.3	7.1	5vs56
Prigi	−94.0	20.9	3vs34	80.0	9.2	4vs45			
Benoa	−233.4	21.8	3vs34				−169.0	15.1	5vs56
Saumlaki									
Waikelo	170.0	42.3	3vs34	197.7	31.7	4vs45	85.8	22.2	5vs56
Booby Island	606.2	85.5	3vs34	86.0	6.9	4vs45	76.4	12.2	6vs6
Milner Bay ("A")				−81.6	6.0	4vs45	−73.7	13.0	6vs6
Groote Eylandt ("B")	−84.6	16.5	3vs4	−57.1	5.3	4vs45	94.9	8.1	6vs7
Darwin	386.4	125.0	3vs4	119.2	16.1	4vs5	−240.0	15.9	6vs67
Wyndham	334.4	98.4	2vs23	255.0	9.1	4vs5	428.2	37.8	5vs56
Port Hedland	−247.6	45.7	3vs4				−97.3	7.5	5vs6
Carnarvon				92.2	12.6	4vs45			
Geraldton	−52.8	20.6	3vs4						
Freemantle									
Bunbury	−65.7	18.8	3vs4				55.0	21.2	5vs56
Albany	−107.1	19.6	3vs4	−104.5	10.0	4vs45	−171.9	1 8.4	5vs56
Esperance	−150.2	29.9	3vs34						
Thevenard	−125.1	41.8	3vs34						
Wallaroo	−143.2	41.3	3vs4				69.4	10.1	6vs7
Port Adelaide (Outer)	173.8	52.5	3vs4	550.0	55.0	4vs45	357.2	40.6	5vs56
Port Adelaide (Inner)	223.3	46.7	3vs4	436.1	41.9	4vs45	351.5	32.9	5vs56
Victor Harbor	−71.8	26.6	3vs34	−65.1	17.3	4vs45	76.0	15.3	6vs67
Portland	−62.5	10.9	3vs4	−73.4	10.3	4vs45	79.2	12.0	6vs67
Point Lonsdale	−83.2	26.9	2vs23	−102.2	8.7	4vs5	−160.5	16.3	5vs56
Williamstown	67.3	31.0	2vs23	95.5	22.2	4vs45	151.5	15.5	5vs56
Stony Point				−90.5	11.0	4vs5	−51.5	17.7	5vs5

Table 5
Continued

Station name	δ-HAT (SA) TACs	δ-HAT (SA) Error	δ-HAT (SA) IMFs	δ-HAT (ANN) TACs	δ-HAT (ANN) Error	δ-HAT (ANN) IMFs	δ-HAT (IA) TACs	δ-HAT (IA) Error	δ-HAT (IA) IMFs
Burnie	**−129.9**	**30.3**	*3vs3*	**−488.4**	**40.5**	*4vs45*	**−210.7**	**42.5**	5vs56
Indian Ocean Islands									
Port Louis							**94.2**	**14.2**	5vs56
Rodrigues	**−71.0**	**21.5**	*2vs23*	**−93.3**	**9.6**	*4vs45*	**−100.9**	**10.6**	6vs67
Reunion "A"	**60.9**	**26.5**	*3vs34*	**76.2**	**9.4**	*4vs45*	**64.4**	**5.1**	6vs7
Reunion "B"									
Point La Rue	**75.2**	**4.6**	*3vs4*	**219.6**	**15.7**	*4vs45*	**82.9**	**17.4**	5vs56
St. Paul							**−84.0**	**23.2**	5vs56
Kerguelen	**−99.3**	**27.1**	*3vs4*	**62.5**	**21.7**	*4vs5*	**207.2**	**44.3**	6vs67
Antarctica									
Syowa Station	**−51.3**	**23.2**	*3vs34*						
Mawson							**−52.9**	**15.0**	5vs6
Davis	**114.8**	**39.2**	*3vs34*				**61.4**	**26.0**	6vs6
Casey	**179.7**	**40.9**	*3vs34*	**−58.3**	**25.6**	*4vs45*			

Notes. Numerical values, their associated errors, and the IMFs mode combinations that gave the "best fit" are given for the sub-annual (SA), annual (ANN), and interannual (IA) frequency bands. IMF mode combinations are listed with the MSL IMF given first. Color shading is used to indicate positive and negative results, and blank entries indicate insignificant results.

Abbreviations: IMFs, intrinsic mode functions; MSL, mean sea level; TACs, tidal anomaly correlations.

IMF combination for the SA band was most often 3vs34 (27), the most common choices in the ANN band were 4vs45 (34), and the most common choice in the IA band was 5vs56. Numerical results for δ-HATs, along with errors, SNRs, and mode combinations chosen are given in Table 5.

4. Discussion

4.1. Summary of Observed Trends

Overall, nearly all locations show a significant TAC in at least one of the three frequency bands, and about half were significant in all three bands. The δ-HAT determinations are also significant at a majority of locations analyzed. The results for O_1 and S_2 generally mirror K_1 and M_2 in geographical distribution but are less often significant, and their IMF combinations were typically similar to that of K_1 and M_2. The ANN band is generally more regionally coherent and of higher magnitude, but the IA band tends to have more locations of significance, and the SA band has less significance in general. The ANN and IA bands were generally more positive than negative for K_1, O_1, and δ-HAT, though M_2 and S_2 were found to be negative slightly more often. By contrast, the SA band was nearly always negative (except for M_2, which was nearly even positive and negative). The IMF mode combinations are most commonly found to have their "best fit" when comparing a single MSL IMF to a combination of tidal IMFs (e.g., MSL_3 vs. X_{34}; MSL_4 vs. X_{45}; MSL_5 vs. X_{56}), which was especially true for the SA and ANN bands; while the IA band often was more well-distributed between all choices, and a clear majority choice was not always seen. This demonstrates that our approach of multiple comparisons is suited to find the relevant timescales of variability.

4.2. Regional Patterns

4.2.1. Arabian Sea Region

We now compare and contrast the patterns seen in each region and discuss some possible mechanisms for the observations. In the Arabian Sea region, both diurnal and semidiurnal tides are of near equal magnitude.

However, the phase structure in the southern Arabian Sea tends to diminish the semidiurnal tides somewhat in the region, while the diurnal tides have nearly equal phase at all locations. The TACs magnitudes are consequently more spatially coherent for diurnal tides than for semidiurnal tides. The K_1 TACs present a pattern that shows an opposing structure of variability that is positive in the Gulf of Aden and within the Persian Gulf, but negative in the Gulf of Oman, suggesting a resonant coupling mechanism between these marginal waters. The M_2 pattern is more consistently negative in the entire sub-region. However, the TAC magnitudes of M_2 are much lower than seen for K_1, so the diurnal component is more important to the region. Although both positive and negative variations are seen in the individual components of tidal amplitudes, the K_1 magnitudes are much larger, and tend to overpower the semidiurnal variabilities, thus, the patterns of the δ-HATs are similar to K_1, more positive in the Gulf of Aden, and more negative in the Gulf of Oman. The annual variability in this region is likely related to the East African monsoon, which brings heavy rain and reverses the trade winds in the western Indian Ocean from December through March (Cook et al., 2012). The annual tidal variations here might change via the yearly fluctuations in MSL caused by monsoonal factors such as rainfall patterns which could influence surface water temperatures and salinity (and thus stratification and mixing). In addition, any year-to-year changes in the strength of the monsoon season, for example, more extreme summer temperatures or wind speeds due to climate change, could likely influence the tidal variability in the IA band.

4.2.2. Bay of Bengal Region

Semidiurnal tides are of generally higher magnitude than diurnal tides in the Bay of Bengal region, though the diurnals are stronger near the western coast of Indian and the Maldives, and in Indonesia. The diurnal TACs inside the Bay of Bengal are negative in nearly all variability modes, while the semidiurnal TACs are positive most places in the region. There are extraordinarily strong and coherent M_2 TACs along the Indonesia coast, in the Maldives, and within the Bay of Bengal, especially in Bangladesh at locations near the Ganges River Delta. There are, however, a few glaring exceptions. Cox's Bazaar is strongly negative, though other nearby locations in Bangladesh within the Ganges Delta are strongly positive. A possible explanation for this may be that this region is also subject to a monsoon season. The Indian monsoon season arrives in June and lasts through October, affecting the Bay of Bengal and the Arabian Sea (Dobler & Ahrens, 2010). Cox's Bazaar is somewhat further from the main Ganges Delta and within a semi-protected harbor, so the river discharge dynamics, which are strongly seasonal and related to the monsoon rainfall, may be more strongly influencing the tidal behavior at the other Bangladeshi locations (especially the ANN band), and Cox's Bazaar might be not as sensitive to river flow. River discharge factors combined with resonance may also help explain why semidiurnal and diurnal TACs are opposed near the Ganges Delta; the rapid increase in local water levels that occur during flood season might lead to a change in resonance that is more “tuned” to semidiurnal wavelengths and less tuned to diurnal wavelengths. Similarly, the large positive TACs seen in the Indonesia island of Sumatra might be due to rainfall and discharge effects, as this mainly mountainous island has many short rivers which rapidly discharge after the intense monsoon rainfall. Since the magnitudes of semidiurnal tides are greater than diurnal tides in these regions, the overall effect of the semidiurnal increase exceeds the decrease in diurnals and leads to an overall increase in tidal range as water level increases.

In the Maldives and at other nearby gauges, the semidiurnal and diurnal TACs are similar, therefore, any increase in MSL should increase the semidiurnal tides and decrease the diurnal tides by a similar amount, balancing the total tidal range. This is confirmed by the patterns of the δ-HATs, which are essentially constant in the Maldives.

4.2.3. African Region

The TAC patterns are most coherent for M_2. With only a few exceptions (e.g., Zanzibar), the M_2 TACs are positive in all frequency bands, with the largest magnitudes generally seen on the southern and northeastern coast. Conversely, the ANN mode of S_2 tends to be moderately negative in most locations, particularly on the Atlantic coast. Though the diurnals are much less in magnitude, the K_1 TACs are also similar to the M_2 patterns, positive nearly everywhere, with some negative IA variability on the Atlantic coast. The largest TACs are seen in the northeastern part of the region, especially near Zanzibar, where the semidiurnal TACs

are strongly negative. The reason for this might be resonance related; this tide gauge is located on an island just off the coast, and the strait between this island and the continent has a larger semidiurnal tide than the surrounding region, which may suggest that the semidiurnal resonance becomes slightly diminished with higher water levels, and the diurnal resonance becomes enhanced. The overall impact on the δ-HAT patterns is a generally positive result at most locations, though the negative ANN variability of S_2 and O_1 at some locations on the Atlantic coast yields a negative ANN band in δ-HAT, and the negative IA variability of M_2 and K_1 yield a negative δ-HAT at the same locations. Also, the negative TACs seen in the semidiurnal tides at Zanzibar are overpowered by the positive trends in K_1, yielding an overall positive δ-HAT here.

4.2.4. Australian Region

In Australia, diurnal tides are generally more dominant. Semidiurnal tides are smaller in most locations due to the presence of amphidromic points along the western coast, though there are regions of higher magnitudes such as the northwestern shelf of Australia, inside the Indonesian waters, and at certain localities along the southern coast. The semidiurnal TACs are mainly insignificant near the amphidromic points, and are generally negative elsewhere in the region, with the exception of Adelaide Harbor, in the Torres Strait (Booby Island), and in Indonesia at Waikelo. Diurnal TACs are generally positive in the ANN and IA band, but consistently negative in the SA band, usually opposed to the semidiurnal TACs in the north and south and being the only significant variability in the west. The strongest magnitude TACs are seen in the central northern regions, especially at Wyndham and Darwin and in the Torres Strait, which have a strong diurnal amplification. There are also strong TACs at Adelaide Harbor and on the Tasman Sea. The overall effect of tidal as expressed by the δ-HATs shows that about half of all locations "balance" the diurnal and semidiurnal variability to yield insignificant δ-HATs, southeastern locations are moderately negative, and very strong positive variability only exists in northern coastal regions and in Adelaide and at Williamstown Harbors. Thus, the δ-HATs seem to be significant only where harbor effects are important in the southern locations, possibly due to changing resonance due to anthropogenic modifications such as channel deepening. The northern locations are likely more influenced by resonant coupling effects between the marginal seas of the Indo-Australian region.

4.2.5. Open Ocean and Antarctic Locations

Antarctica is mainly dominated by diurnal tides, since semidiurnal tides become quite small in polar regions. A strong coherency of K_1 TACs on the southern landmass (and at Kergulen Island) is a consequence of the diurnal dominance. The variability of the ANN band is particularly strong. In this part of the world, an obvious factor that acts seasonally would be the cycle of sea ice formation and melting, which may be influencing the magnitude of diurnal tides; indeed, tides are of course larger when ice is melting, as the water surface can rise and fall more freely; less so while frozen. However, negative trends in S_2 and O_1 lead to overall insignificant δ-HATs in Antarctica.

At the remainder of the Indian island gauges, we see a mixed pattern. There is a strong positive bias in all TAC bands at Point La Rue in the north for K_1, and slightly negative in the Seychelles further south. The M_2 TACs also are strongly positive Point La Rue as well as for the early data of Reunion Island and at Port Louis Islands in the Seychelles, but negative east of this. A similar pattern is seen in S_2. A possible explanation for this might be a movement of the amphidromic points. Amphidromic migration mechanisms have been discussed in previous studies (see, e.g., Pickering, 2012; Pugh, 2004), and are typically thought of as a consequence of sea level rise redistributing resonance between diurnal and semidiurnal tides within an ocean basin. We notice from Figures 5 and 7 that the Seychelles are in a region of tightly space phase lines aligned with the local amphidromic points in both K_1 and M_2. Point La Rue, on the other hand, is a bit nearer to the amplification region of both tidal constituents. If we suppose that the amphidromic point of K_1 has moved eastward over time as sea levels have risen, this would expand the amplification region of K_1 in the Arabian Sea, increasing the tidal amplitudes at Point La Rue and lessening them in the Seychelles. If the M_2 amphidromic point also migrated eastward, this might extend the high amplitude region in the Mozambique Channel east and north and diminish the high-amplitude region seen in the middle of the Indian Ocean. Such a motion would suggest an increase of M_2 amplitudes at point La Rue and in the Seychelles and a decrease at the eastern islands, which would match with what is observed. A final point of interest that might support this hypothesis is seen when looking at the δ-HAT map is that the fact that Point La Rue is strongly positive

due to strong increases in K_1 and M_2 TACs and Rodrigues Island is moderately negative. It may be possible that the generally negative semidiurnal TACs seen on the northwest shelf of Australia might be partially due to a northward migration of the amphidromic points, which would diminish tidal amplitudes there.

4.3. Differences in TAC Behavior Over Time

Of the 73 locations that we surveyed in this study, 15 were split into early ("A") and later ("B") data sets. Comparison of the results between the early and late data may provide an insight of any changes in the behavior of tidal variability over time. The majority of locations that were split into two data sets had similar behavior in both records. There are some notable exceptions, however. Most of the "A" and "B" stations are found in South Africa; as mentioned above, this tide gauge network fell into disrepair in the 1990s and was later re-established in the 2000s with updated instruments. A few gauges do show a difference between time eras in the ANN band, and about half show a divergence in the IA band, especially for S_2. However, the rest of the records are mainly consistent, so it is not probable that the instrumental changes introduced the differences, as this would manifest as a systematic difference seen at all locations. In the Bay of Bengal region, "A" and "B" records generally show consistence in semidiurnal tides, even at Colombo, where there is a large gap between the early and late data (~40 years). However, the early and later data diverge in behavior for diurnal tides, especially in K_1, which shows a different signature in all three bands. We suggest three possible reasons for this. The first might be a migration of the diurnal amphidromic point near Sri Lanka, though this would likely change the TACs more uniformly across the frequency bands. The second possibility is that the 2004 Sumatra earthquake and resulting motion of the oceanic crust might have shifted the basin structure enough the slightly change the tidal characteristics of the diurnal tides in the region. The third possibility is that, because of the earthquake, the tide gauges in this region were updated in the mid-2000s (when the "B" records begin), and improved instrumentation may be yielding slightly different water level recordings.

4.4. Importance of the Annual Mode of Variation

We have demonstrated that is, possible to estimate tidal variability from short-record tide gauges and can determine significant trends at multiple time scales using the EEMD method, which has provided an improvement on previous methods employing the TAC approach. We considered three general scales of variability: SA, ANN, and IA. The SA band captures processes that are important on a monthly scale, the ANN band captures yearly related mechanisms (such as monsoon cycles), and the IA band captures lower-mode variations occurring over several years or more. Our results here show that the largest number of locations was significant in the IA band, though the magnitudes were often small. This may be that since most of the data considered here were of short record (12 years or less), it was too difficult for the EEMD calculations to accurately determine the IA variability, which could be on frequency scales of 2–10 years, and might only capture a few cycles. On the other end of the spectrum, the SA band did show some large magnitude TACs at some locations (e.g., Wyndham and Darwin, Australia), but most locations were of a lesser magnitude. Therefore, in our approach here and for our chosen data set, the most important and consistently large magnitude timescale of variability is the ANN band.

In standard monthly tidal harmonic analysis, the annual tides cannot be removed, and it is expected to see a strong yearly cycle. However, using our approach of tidal admittance, where we remove the majority of the gravitationally related yearly cycle via the tidal potential, it is assumed that the large part of the yearly variability that remains is due to terrestrial factors, such as weather and climate. This means that retaining the variability present in the ANN band of our EEMD calculations allows us to further analyze climate factors that may be influencing tidal properties on a yearly scale. The ANN band is especially important in many parts of the Indian Ocean region, where strong annual cycles such as changing patterns of the monsoon winds and rains are the dominant climate force. This generally leads to times of higher water levels and lower water levels over the course of each year. However, the timing of these events can vary significantly over a large geographical area. Rainy seasons that occur in certain regions can lead to a delayed river discharge in other regions along with delays in the setup of the persistent monsoonal winds can lead to a temporal difference in when coastal areas see water levels increase. The TAC method shows that tidal amplitudes also can be influenced by water level changes, and should also exhibit a yearly cycle, which might be more

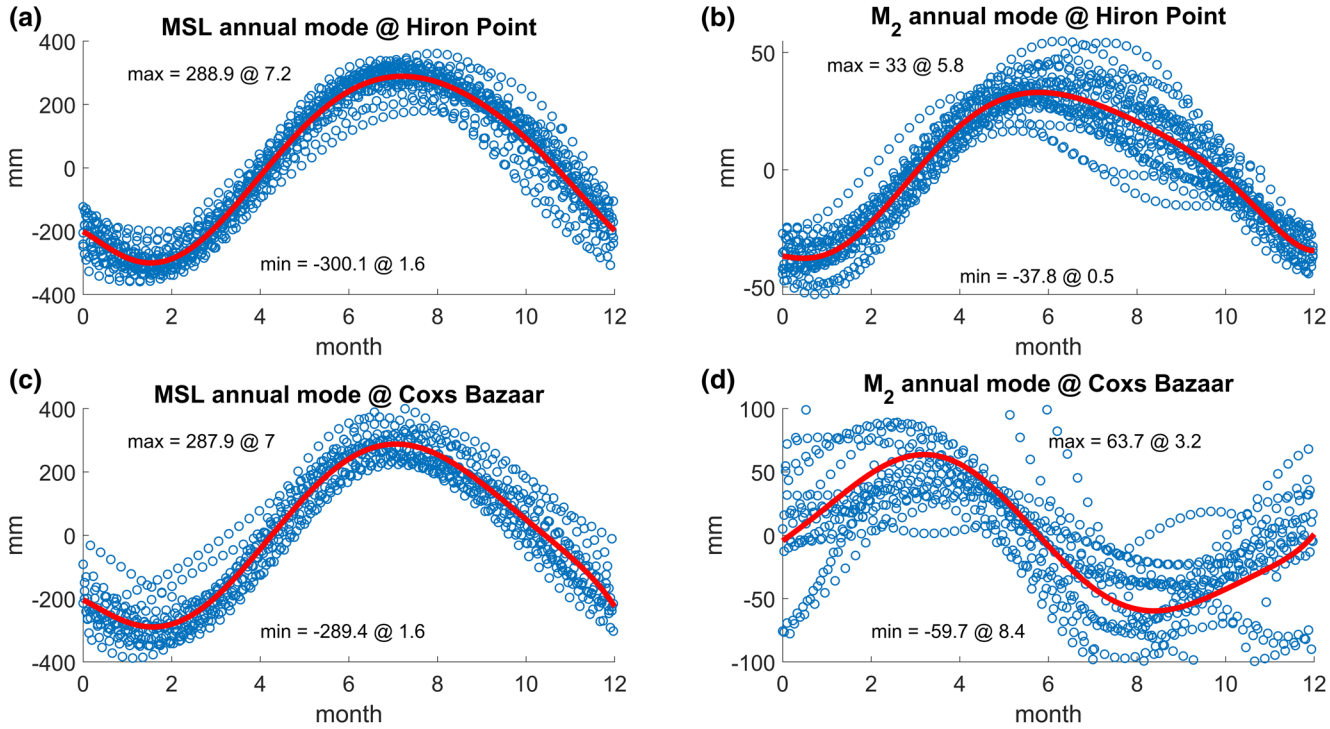

Figure 11. Yearly patterns of the annual mode of mean sea level (intrinsic mode function [IMF] #4) at Hiron Point (a) and Cox's Bazaar (c), Bangladesh, and the yearly patterns of the annual mode of M_2 (IMF #4 + #5) at the same locations (b and d). All data are collapsed into month-of-year and each year of the record is shown as the overlapping blue dots. Red lines are a high-order polynomial fit to the scattered data. Text in each subplot indicates the maximum and minimum of each fit (units of millimeter), along with occurrence of extrema (month number to nearest tenth).

extreme in monsoon regions. Therefore, the most important concern for coastal flooding is an understanding of when MSL will reach peaks levels, and when tidal amplitudes can be expected to peak. Therefore, it will be instructive to look closer at the variability of the annual modes of tides and MSL captured by the EEMD process. We consider two stations in the Bay of Bengal region and two stations in the Arabian Sea region which had opposing TAC responses. We revisit the ANN IMFs (which was IMF #4 for MSL, and for tides was IMFs #4 + #5 at the stations of interest). The year value of time in each record is stripped off, and we scatterplot each determination of MSL and tides to produce a climatology of the yearly cycle by month, with each year of the record overlapping each other to reveal the yearly patterns. These curves are fitted with a high-order polynomial to yield an estimate for the average yearly cycle and determine the average maximum and minimum value of this curve as well as their timing during the year. In the Bay of Bengal, we use the M_2 results from Hiron Point (positive TAC), and Cox's Bazaar (negative TAC), which covered a similar time period, plotted in Figure 11. In the Arabian Sea, we use the K_1 TAC results of Aden and Muscat, which had positive and negative TACs, respectively, shown in Figure 12. In both plots, the blue scattered points are the original data of the ANN IMFs, and the red lines are the fits. The maximum and minimum values, as well as the month number of occurrences of maxima and minima are included on each subplot.

In the Bay of Bengal (Figure 11), the ANN mode of MSL is similar at both Hiron Point and Cox's Bazaar, with maximum values of about 288 mm reached in early July, and minimum values of about −290 mm in mid-January at both locations. This is not surprising, as the Indian monsoon affects both locations with a similar intensity and timing. However, the response of M_2 is much different at the two locations. At Hiron Point, the M_2 ANN mode looks similar to MSL, and experiences both its maximum (33 mm) and its minimum (−38 mm) about a month and half before the maximum in MSL. At Cox' Bazaar, however, the M_2 maximum (64 mm) happens in March, a few months after the MSL minimum, and the M_2 minimum comes in August, shortly after the MSL maximum. Thus, there is a clearly reversed relationship between the two forms of water level variability at Cox' Bazaar, while at Hiron Point, they are essentially in sync. In terms of total water levels, this would suggest that Hiron Point would be much more vulnerable to the impacts

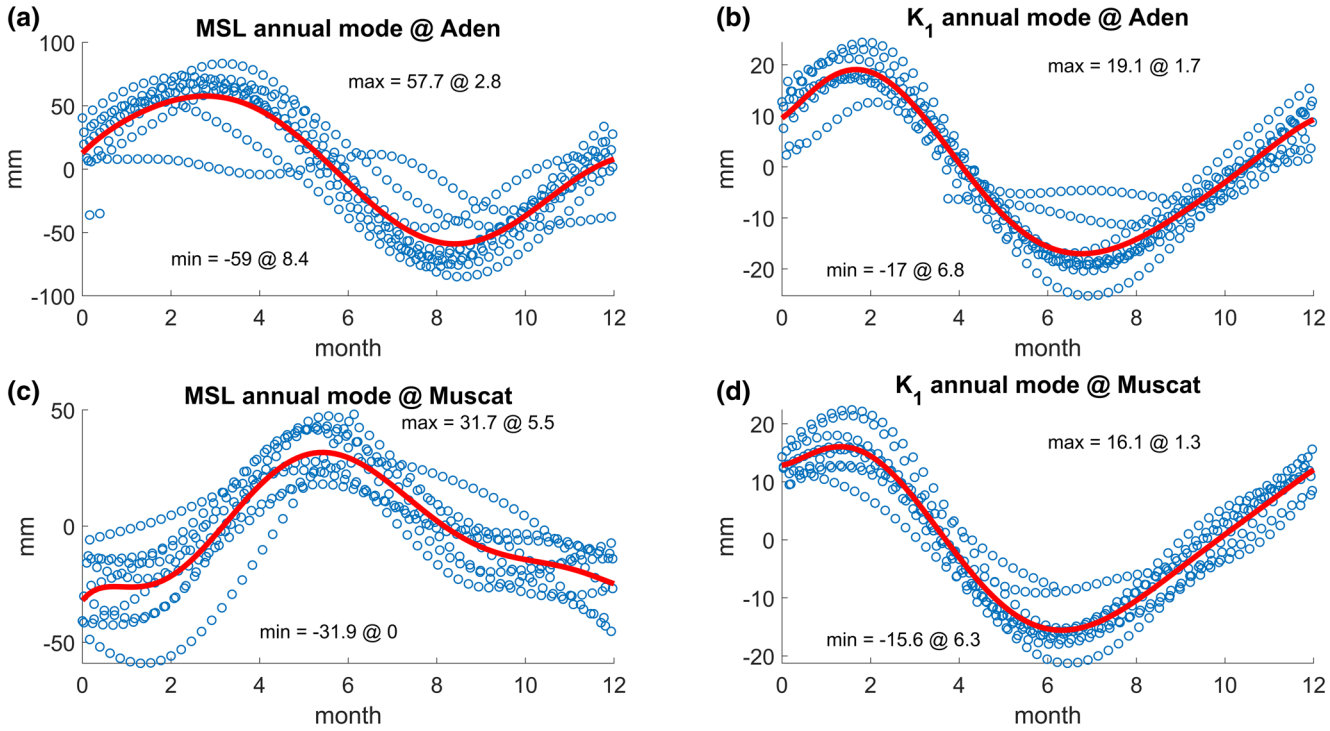

Figure 12. Yearly patterns of the annual mode of mean sea level (intrinsic mode function [IMF] #4) at Aden, Yemen (a) and Muscat, Oman (c), and the yearly patterns of the annual mode of K_1 (IMF #4 + #5) at the same locations (b and d). All data are collapsed into month-of-year and each year of the record is shown as the overlapping blue dots. Red lines are a high-order polynomial fit to the scattered data. Text in each subplot indicates the maximum and minimum of each fit (units of millimeter), along with occurrence of extrema (month number to nearest tenth).

of yearly flooding than at Cox' Bazaar, as the maximum impact of tides and MSL would be additive at the former, and would work against each other at the latter. One reason for this response might be because even though these locations are close to each other, they are in different environments. Hiron Point is soundly within the Ganges River delta, and the tides here are likely subject to direct influence from the extreme run-off events that occur seasonally. Cox's Bazaar, on the other hand, is further from the Ganges delta, within a semi-enclosed harbor location. This distance between locations, albeit short, might be sufficient to yield a different response in the M_2 tide to annual MSL variations. Alternatively, it could be due to a reflection of the incoming M_2 tide in the semi-enclosed bay in the northeast part of the Bay of Bengal north of Cox's Bazaar that gives it a different phase here, or the phase could possibility shift as the incoming tide moves clockwise from the west to the east along the Indian and Bangladeshi coast. There is a complex bunching of phase lines in this region, so this is a reasonable possibility. Moulmein, Myanmar also has negative TACs, and is also on the eastern side of the Andaman Sea, with a complex bunching of phase lines. A similar tidal reflection mechanism might also be at play here.

We see a much different pattern in the Arabian Sea region (Figure 12). Here, the timing and magnitude of the ANN mode of the K_1 tide is nearly identical at both Aden and Muscat, with a maximum in mid-January of about 17 mm, and a minimum in mid-June of about −16 mm. However, in this region, it is the MSL patterns that are reversed between locations. At Aden, MSL has a maximum of about 58 mm in late February, and a minimum of about −59 mm in mid-August, thus the yearly cycle of tides leads that of MSL by about a month. Conversely, at Muscat, MSL reaches a maximum of about 32 mm during mid-May, and a minimum of about −322 mm in early January. Comparing to the maximum and minimum of the K_1 tide, this pattern is nearly exactly reversed. Thus, in this region, Aden would be susceptible to tide-induced flooding, as the extrema in MSL and tidal amplitudes are closely in sync, while at Muscat, they would work against each other.

This exercise has highlighted the importance of the annual mode of variations in monsoon-affected areas. In both regions considered here, we found tide gauge locations that showed opposing TACs. At Hiron Point in

the Bay of Bengal, and at Aden in the Arabian Sea, we observed a positive TAC in M_2, and K_1, respectively. However, even though the overall variability of both MSL and the dominant tide was in sync, the yearly patterns were different, that is, Hiron Point has its maximum value in both MSL and M_2 during summer, while Aden reached its maxima in MSL and in K_1 during winter. In both cases, the maxima in MSL are related to the associated maxima in yearly rainfall at each location, and at both locations, the tides also reach their maxima nearly in sync. However, at the other locations analyzed, Cox's Bazaar in the Bay of Bengal, and Muscat in the Arabian Sea, we see a negative TAC, but for different reasons. At Cox's Bazaar, the yearly MSL is identical to that at Hiron Point, and the tides are reversed, but at Muscat, the yearly mode of the tides are identical to Aden, and the yearly MSL pattern is reversed. The difference in MSL may be due to the influence of different monsoon systems; Muscat and the eastern part of the Arabian Sea is more controlled by the Indian Monsoon, while Aden and the western parts of the Arabian Sea are more influenced by the East African monsoon, and each annual MSL mode reflects each region's dominant rainfall patterns. However, this difference also shows that the response of tides may not always be completely bound to the patterns of MSL, as regional tidal patterns may overpower the effects of local MSL changes. We recall from Figure 8a that in the Arabian Sea, the phase of the K_1 tide is nearly simultaneous at all locations, which is different than the tidal phases of M_2 in the Bay of Bengal (Figure 8b), as there is a complex compact region of phase lines near the Ganges Delta, so this might explain the opposing responses of the M_2 tide to an identical MSL pattern in the Bay of Bengal and the similar response of the K_1 tide in different sub-regions of the Arabian Sea to a differing MSL input. Alternatively, the explanations for the difference in tidal behaviors may be partially related to river flow, as one of the locations in the Bay of Bengal is within influencing distance of the Ganges River Delta and its massive seasonal outflow, while the locations in the Arabian Sea are not river-influenced. This mechanism, however, would not explain the differences in TACs between Arabian Sea locations.

5. Conclusions and Future Research

This study has carried out a survey of tidal variability in the Indian Ocean, using a combination of the well-demonstrated TAC method and an EEMD technique to determine and catalog multiple timescales of variability, namely, the SA, ANN, and IA bands. The benefits of this study are twofold. First, we have provided insight into the nature of tidal variability in an area of the world ocean where tidal properties have not been previously studied in depth due to a historical lack of data, and have shown that tides may act very differently in different sub-regions and at different timescales. Second, we have demonstrated the usefulness of the EEMD approach when combined with the TAC method to analyze short-record tide gauge data, and the ability of this methodology to differentiate and compare multiple modes of variability separately.

Our results showed that nearly all locations analyzed showed significant TACs in at least one frequency band (SA, ANN, or IA), with about half of all locations being significant in all three bands in at least one of the major tides. Interestingly, some locations exhibit a different trend in different bands (e.g., some are positive in the SA or ANN band but negative in the IA band, or vice versa). This suggests that tides and MSL can be influenced by multiple mechanisms active at different timescales. For instance, the ANN band is often related to the yearly monsoon cycles and associated mechanisms (such as river discharge) in certain regions, but the IA band may be more closely related to other forms of climate variability which have natural variations of a few years. We also revealed some regional coherence of tidal variability. The diurnal tides (especially K_1) and their TACs are the dominant factor with the largest variability in the Arabian Sea, in most of Australia, and in Antarctica, while the semidiurnal tides (especially M_2) and their TACs are more dominant in the Bay of Bengal and along most of the African coast. The results from the δ-HAT analyses generally showed significant but small-to-moderate magnitude results, though there were some local exceptions to this generalization. Adelaide, Wyndham, and Williamstown in Australia had exceptionally large positive δ-HATs. Large positive δ-HATs were found in semi-enclosed regions where local tidal resonances and harbor modifications may be responsible for the large changes in tides; a similar result was seen in Hong Kong in its developed harbor regions (Devlin et al., 2019b). Other locations of note that have large δ-HATs include the northeastern coast and the southern tip of Africa, the Ganges Delta, and parts of the Indonesia coast. All of these locations may experience higher tidal ranges under future scenarios of rising MSLs, which will be especially impactful in areas that are densely populated.

This study has also demonstrated the effectiveness of separating the annual mode to look at the nature of the yearly patterns of tidal and sea level variations. This was demonstrated by the example of comparing stations with different sign TACs in the Bay of Bengal and the Arabian Sea, which showed that sometimes MSL can be similar across a region, and the tides can have a different response (as seen for M_2 in the Bay of Bengal), and in other cases, the tides can be uniform in a region, but different locations can experience different MSL behavior during the year (as seen for K_1 in the Arabian Sea).

To fully determine the reasons for the forms of variability observed here, more work is needed, including numerical modeling of different processes to see their influence on the tides, this will be performed in future studies. The results from each frequency band found here may give clues as to which mechanisms are most likely; for example, monthly and other short-term processes such as extreme weather events are likely are more important to the SA band, annual and seasonal processes such as monsoons are more significant to the ANN band, and multiyear variability, such as seen by climate patterns like the El Nino Southern Oscillation will be more closely related to the IA band. Exploring the dynamics of monsoon related variability in the Bay of Bengal and Arabian Sea will be of particular interest, as the likely causative mechanisms are well-known and relatively easily modeled. An upcoming study will simulate the various mechanisms in a tidal model that may lead to the observed tidal variability. In particular, we will design focused regional studies of some of the sub-regions most impacted by monsoonal variability and where the most interesting observations of tidal/MSL correlations were found. In particular, we will examine the Bay of Bengal and the Arabian Sea, and analyze the effects of seasonal wind variability, frictional changes in different season in shallow-water regions, and seasonal rainfall variability, which may induce seasonal river runoff and seasonal stratification, which may in turn, may influence tidal mixing, internal wave dynamics. A similar modeling study was previously carried out (Devlin et al., 2018), where 2D barotropic numerical models were performed in the Southeast Asian region, another region strongly affected by monsoons, and this effort achieved satisfactory results to explain the observed mechanisms. Our intended models of the Indian Ocean sub-regions will build on the previous study, but will include 3D considerations such as baroclinicity, stratification, and mixing, and will also integrate observations from bottom pressure recorders and satellite altimetry observations of tides and MSL in the Indian Ocean. We hope that these models will help to clear up some of the unanswered questions found by this current study, such as why the yearly characteristics of the M_2 tide are much different at Hiron Point and Cox's Bazaar, and why MSL in the Arabian Sea can vary so much between nearby locations.

The success demonstrated by the coupled TAC/EEMD method also invites a return to locations in the Pacific and Atlantic Oceans studied in past works. Since we previously required a record length of 20 years to yield significant results from yearly analyses, many shorter-record locations were not considered, which left some "holes" in the geographical coverage of the ocean which might now be overcome via our new methods. Using the new method described here, we could now revisit these shorter record gauges to make new determinations of tidal variability, and compare to past results at nearby longer record tide gauges to improve the understanding of tidal variability in the entire world ocean. This combined approach could also be applied to other instrumental observations of water level besides coastal tide gauges, such as bottom pressure recorders or moored surface current observations, which often only have a few years of data available to analyze.

Conflict of Interest Statement

The authors declare they have no competing interests.

Author Contributions

Adam T. Devlin did all analyses, figures, tables, the majority of writing, and complied the manuscript. Jiayi Pan provided editing, insight, guidance, and direction to this study. Hui Lin provided critical insight and helpful input.

Data Availability Statement

The majority of original hourly tide gauge data used in this study is acquired freely from the University of Hawai'i Sea Level Center (https://uhslc.soest.hawaii.edu/). Other data are provided by the Global Extreme Sea Level Analysis project (GESLA, https://gesla.org/). The data from GESLA have two components, a public archive which is freely available for download, and a "private" archive of Australian data which require contacting the administrators. Our study uses a small number of data records from this "private" archive, after direct communication with the relevant administrators.

Acknowledgments
This work is supported by the General Research Fund of Hong Kong Research Grants Council (RGC) (CUHK 14303818), the National Natural Science Foundation of China (project 41376035 and U1811464), and the talent startup fund of Jiangxi Normal University.

References

Akbari, P., Sadrinasab, M., Chegini, V., & Siadatmousavi, M. (2016). Tidal constituents in the Persian Gulf, Gulf of Oman and Arabian Sea: A numerical study. *Indian Journal of Geo-Marine Sciences*, *45*(8), 1010–1016.

Amin, M. (1983). On perturbations of harmonic constants in the Thames Estuary. *Geophysical Journal International*, *73*(3), 587–603.

Arbic, B. K. (2005). Atmospheric forcing of the oceanic semidiurnal tide. *Geophysical Research Letters*, *32*, L02610. https://doi.org/10.1029/2004GL021668

Arbic, B. K., Karsten, R. H., & Garrett, C. (2009). On tidal resonance in the global ocean and the back-effect of coastal tides upon open-ocean tides. *Atmosphere-Ocean*, *47*(4), 239–266. https://doi.org/10.3137/OC311.2009

Arns, A., Dangendorf, S., Jensen, J., Bender, J., Talke, S. A., & Pattiaratchi, C. (2017). Sea-level rise induced amplification of coastal protection design heights. *Nature: Scientific Reports*, *7*, 40171. https://doi.org/10.1038/srep40171

Buchanan, M. K., Oppenheimer, M., & Kopp, R. E. (2017). Amplification of flood frequencies with local sea level rise and emerging flood regimes. *Environmental Research Letter*, *12*, 6. https://doi.org/10.1088/1748-9326/aa6cb3

Cartwright, D. E. (1972). Secular changes in the oceanic tides at Brest, 1711–1936. *Geophysical Journal International*, *30*(4), 433–449.

Cartwright, D. E., & Tayler, R. J. (1971). New computations of the tide-generating potential. *Geophysical Journal of the Royal Astronomical Society*, *23*, 45–74. https://doi.org/10.1111/j.1365-246X.1971.tb01803.x

Cheng, Y., Ezer, T., Atkinson, L. P., & Xu, Q. (2017). Analysis of tidal amplitude changes using the EMD method. *Continental Shelf Research*, *148*, 44–52. https://doi.org/10.1016/j.csr.2017.09.009

Chernetsky, A. S., Schuttelaars, H. M., & Talke, S. A. (2010). The effect of tidal asymmetry and temporal settling lag on sediment trapping in tidal estuaries. *Ocean Dynamics*, *60*, 1219–1241. https://doi.org/10.1007/s10236-010-0329-8

Cherqui, F., Belmeziti, A., Granger, D., Sourdril, A., & Le Gauffre, P. (2015). Assessing urban potential flooding risk and identifying effective risk-reduction measures. *The Science of the Total Environment*, *514*, 418–425.

Church, J. A., Hunter, J. R., McInnes, K. L., & White, N. J. (2006a). Sea-level rise around the Australian coastline and the changing frequency of extreme sea-level events. *Australian Meteorological Magazine*, *55*(4), 253–260.

Church, J. A., & White, N. J. (2011). Sea Level rise from the late 19th to the early 21st century. *Surveys in Geophysics*, *32*(4), 585–602. https://doi.org/10.1007/s10712-011-9119-1

Church, J. A., & White, N. J. (2006). A 20th century acceleration in global sea level rise. *Geophysical Research Letters*, *33*, L01602. https://doi.org/10.1029/2005GL024826

Church, J. A., White, N. J., & Hunter, J. R. (2006b). Sea-level rise at tropical Pacific and Indian Ocean islands. *Global and Planetary Change*, *53*(3), 155–168.

Clarke, A. J., & Liu, X. (1994). Interannual sea level in the northern and eastern Indian Ocean. *Journal of Physical Oceanography*, *24*(6), 1224–1235.

Colossi, J. A., & Munk, W. (2006). Tales of the venerable Honolulu tide gauge. *Journal of Physical Oceanography*, *36*, 967–996. https://doi.org/10.1175/JPO2876.1

Cook, K. H., Meehl, G. A., & Arblaster, J. M. (2012). Monsoon regimes and processes in CCSM4. Part II: African and American monsoon systems. *Journal of Climate*, *25*(8), 2609–2621.

Dangendorf, S., Marcos, M., Wöppelmann, G., Conrad, C. P., Frederikse, T., & Riva, R. (2017). Reassessment of 20th century global mean sea level rise. *Proceedings of the National Academy of Sciences*, *114*(23), 201616007.

Devlin, A. T., Jay, D. A., Talke, S. A., & Zaron, E. (2014). Can tidal perturbations associated with sea level variations in the western Pacific Ocean be used to understand future effects of tidal evolution?. *Ocean Dynamics*, *64*(8), 1093–1120. https://doi.org/10.1007/s10236-014-0741-6

Devlin, A. T., Jay, D. A., Talke, S. A., Zaron, E. D., Pan, J., & Lin, H. (2017b). Coupling of sea level and tidal range changes, with implications for future water levels. *Scientific Reports*, *7*(1), 17021. https://doi.org/10.1038/s41598-017-17056-z

Devlin, A. T., Jay, D. A., Zaron, E. D., Talke, S. A., Pan, J., & Lin, H. (2017a). Tidal variability related to sea level variability in the Pacific Ocean. *Journal of Geophysical Research: Oceans*, *122*(11), 8445–8463. https://doi.org/10.1002/2017JC013165

Devlin, A. T., Pan, J., & Lin, H. (2019a). Extended spectral analysis of tidal variability in the North Atlantic Ocean. *Journal of Geophysical Research: Oceans*, *124*(1), 506–526. https://doi.org/10.1029/2018JC014694

Devlin, A. T., Pan, J., & Lin, H. (2019b). Tidal variability in the Hong Kong region. *Ocean Science*, *15*(4), 853–864.

Devlin, A. T., Zaron, E. D., Jay, D. A., Talke, S. A., & Pan, J. (2018). Seasonality of tides in Southeast Asian waters. *Journal of Physical Oceanography*, *48*(5), 1169–1190. https://doi.org/10.1175/JPO-D-17-0119.1

Dobler, A., & Ahrens, B. (2010). Analysis of the Indian summer monsoon system in the regional climate model COSMO-CLM. *Journal of Geophysical Research*, *115*(D16), 1–12. https://doi.org/10.1029/2009JD013497

Domingues, C. M., Church, J. A., White, N. J., Glecker, P. J., Wijffels, S. E., Barker, P. M., & Dunn, J. R. (2008). Improved estimates of upper-ocean warming and multi-decadal sea level rise. *Nature*, *453*, 1090–1094. https://doi.org/10.1038/nature07080

Dube, S. K., Jain, I., Rao, A. D., & Murty, T. S. (2009). Storm surge modelling for the Bay of Bengal and Arabian Sea. *Natural Hazards*, *51*(1), 3–27.

Egbert, G. D., & Erofeeva, S. Y. (2002). Efficient inverse modeling of barotropic ocean tides. *Journal of Atmospheric and Oceanic Technology*, *19*(2), 183–204.

Emery, K. O., & Aubrey, D. G. (1989). Tide gauges of India. *Journal of Coastal Research*, *5*(3), 489–501.

Familkhalili, R., & Talke, S. A. (2016). The effect of channel deepening on tides and storm surge: A case study of Wilmington, NC. *Geophysical Research Letters*, *43*(17), 9138–9147. https://doi.org/10.1002/2016GL069494

Feng, A., & Deng, Y. (2018). The 21st century Maritime Silk Road A perspective from China on a network of free trade areas. From: "21st century Maritime Silk Road". In J. Randall, L. Brinklow, L. Liyun, & C. Qinhing. *The 21st Century Maritime Silk Road Islands Economic Cooperation Forum ANNUAL REPORT ON GLOBAL ISLANDS 2018* (pp. 205–226). Prince Edward Island, CA: Island Studies Press at UPEI. ISBN 978-1-988692-28-9 (digital).

Feng, X., Tsimplis, M. N., & Woodworth, P. L. (2015). Nodal variations and long-term changes in the main tides on the coasts of China. *Journal of Geophysical Research: Oceans*, *120*(2), 1215–1232. https://doi.org/10.1002/2014JC010312

Godin, G. (1986). Is the abnormal response of the tide at the frequency of S2 really due to radiational effects?. *Continental Shelf Research*, *6*(5), 615–625.

Godin, G. (1991). Frictional effects in river tides. *Tidal Hydrodynamics*, *379*, 402.

Green, J. A. M. (2010). Ocean tides and resonance. *Ocean Dynamics*, *60*(5), 1243–1253.

Guo, L., van der Wegen, M., Jay, D. A., Matte, P., Wang, Z. B., Roelvink, D., & He, Q. (2015). River-tide dynamics: Exploration of nonstationary and nonlinear tidal behavior in the Yangtze River estuary. *Journal of Geophysical Research: Oceans*, *120*(5), 3499–3521. https://doi.org/10.1002/2014JC010491

Haigh, I. D., Eliot, M., & Pattiaratchi, C. (2011). Global influences of the 18.61 year nodal cycle and 8.85 year cycle of lunar perigee on high tidal levels. *Journal of Geophysical Research*, *116*, C06025. doi: https://doi.org/10.1029/2010JC006645

Haigh, I. D., Eliot, M., Pattiaratchi, C., & Wahl, T. (2011). Regional changes in mean sea level around Western Australia between 1897 and 2008. In *Coasts and ports 2011: Diverse and developing: Proceedings of the 20th Australasian coastal and ocean engineering conference and the 13th Australasian Port and Harbour conference* (pp. 280) Engineers Australia.

Haigh, I. D., Pickering, M. D., Green, J. M., Arbic, B. K., Arns, A., Dangendorf, S., et al. (2020). The tides they are A-changin': A comprehensive review of past and future nonastronomical changes in tides, their driving mechanisms, and future implications. *Reviews of Geophysics*, *58*(1), e2018RG000636. https://doi.org/10.1029/2018RG000636

Haigh, I. D., Wijeratne, E. M. S., MacPherson, L. R., Pattiaratchi, C. B., Mason, M. S., Crompton, R. P., & George, S. (2014). Estimating present day extreme water level exceedance probabilities around the coastline of Australia: Tides, extra-tropical storm surges and mean sea level. *Climate Dynamics*, *42*(1–2), 121–138.

Han, W., Meehl, G. A., Rajagopalan, B., Fasullo, J. T., Hu, A., Lin, J., et al. (2010). Patterns of Indian Ocean sea-level change in a warming climate. *Nature Geoscience*, *3*(8), 546–550.

Holleman, R. C., & Stacey, M. T. (2014). Coupling of sea level rise, tidal amplification, and inundation. *Journal of Physical Oceanography*, *44*(5), 1439–1455.

Huang, N. E., Shen, Z., Long, S. R., Wu, M. C., Shih, H. H., Zheng, Q., et al. (1998). The empirical mode decomposition and the Hilbert spectrum for nonlinear and non-stationary time series analysis. *Proceedings of the Royal Society of London. Series A: Mathematical, Physical and Engineering Sciences*, *454*(1971), 903–995.

IO COMISSION (2007). *Ocean data and information network for Africa (ODINAFRICA)*.

Jay, D. A. (2009). Evolution of tidal amplitudes in the eastern Pacific Ocean. *Geophysical Research Letters*, *36*, L04603. https://doi.org/10.1029/2008GL036185

Jay, D. A., Leffler, K., & Degens, S. (2011). Long-term evolution of Columbia river tides. *ASCE Journal of Waterway, Port, Coastal, and Ocean Engineering*, *137*, 182–191. https://doi.org/10.1061/(ASCE)WW.19435460.0000082

Kämpf, J., & Sadrinasab, M. (2006). The circulation of the Persian Gulf: A numerical study. *Ocean Science*, *2*, 27–41. www.ocean-sci.net/2/27/2006/

Kang, S. K., Chung, J. Y., Lee, S. R., & Yum, K. D. (1995). Seasonal variability of the M2 tide in the seas adjacent to Korea. *Continental Shelf Research*, *15*(9), 1087–1113.

Leffler, K. E., & Jay, D. A. (2009). Enhancing tidal harmonic analysis: Robust (hybrid L1/L2) solutions. *Continental Shelf Research*, *29*(1), 78–88.

Mawdsley, R. J., Haigh, I. D., & Wells, N. C. (2015). Global changes in tidal high water, low water and range. *Earth's Futures*, *3*(2), 66–81. https://doi.org/10.2112/SI70-058.1

Merrifield, M. A., Merrifield, S. T., & Mitchum, G. T. (2009). An anomalous recent acceleration of global sea level rise. *Journal of Climate*, *22*(21), 5772–5781.

Moftakhari, H. R., AghaKouchak, A., Sanders, B. F., Allaire, M., & Matthew, R. A. (2018). What is nuisance flooding? Defining and monitoring an emerging challenge. *Water Resources Research*, *54*(7), 4218–4227.

Moftakhari, H. R., AghaKouchak, A., Sanders, B. F., Feldman, D. L., Sweet, W., Matthew, R. A., & Luke, A. (2015). Increased nuisance flooding along the coasts of the United States due to sea level rise: Past and future. *Geophysical Research Letters*, *42*(22), 9846–9852. https://doi.org/10.1002/2015GL066072

Moftakhari, H. R., AghaKouchak, A., Sanders, B. F., & Matthew, R. A. (2017). Cumulative hazard: The case of nuisance flooding. *Earth's Future*, *5*(2), 214–223. https://doi.org/10.1002/2016EF000494

Müller, M. (2011). Rapid change in semi-diurnal tides in the North Atlantic since 1980. *Geophysical Research Letters*, *38*(11), 1–6. https://doi.org/10.1029/2011GL047312

Müller, M. (2012). The influence of changing stratification conditions on barotropic tidal transport. *Continental Shelf Research*, *47*(15), 107–188. https://doi.org/10.1016/j.csr.2012.07.003

Müller, M., Arbic, B. K., & Mitrovica, J. X. (2011). Secular trends in ocean tides: Observations and model results. *Journal of Geophysical Research*, *116*(C5), 1–19. https://doi.org/10.1029/2010JC006387

Müller, M., Cherniawsky, J. Y., Foreman, M. G. G., & Storch, J. S. (2012). Global M2 internal tide and its seasonal variability from high resolution ocean circulation and tide modeling. *Geophysical Research Letters*, *39*(19). https://doi.org/10.1029/2012GL053320

Munk, W. H., & Cartwright, D. E. (1966). Tidal spectroscopy and prediction. *Philosophical Transactions of the Royal Society of London A: Mathematical, Physical and Engineering Sciences*, *259*(1105), 533–581.

Nagarajan, B., Suresh, I., Sundar, D., Sharma, R., Lal, A. K., Neetu, S., et al. (2006). The great tsunami of 26 December 2004: A description based on tide-gauge data from the Indian subcontinent and surrounding areas. *Earth Planets and Space*, *58*(2), 211–215.

Nerem, R. S., Chambers, D. P., Choe, C., & Mitchum, G. T. (2010). Estimating mean sea level change from the TOPEX and Jason altimeter missions. *Marine Geodesy*, *33*(S1), 435–446. https://doi.org/10.1080/01490419.2010.491031

Pawlowicz, R., Beardsley, B., & Lentz, S. (2002). Classical tidal harmonic analysis including error estimates in MATLAB using T_TIDE. *Computers and Geosciences*, *28*(8), 929–937.

Pelling, H. E., & Green, J. M. (2014). Impact of flood defences and sea-level rise on the European Shelf tidal regime. *Continental Shelf Research*, *85*, 96–105.

Pelling, H. E., Green, J. M., & Ward, S. L. (2013b). Modelling tides and sea-level rise: To flood or not to flood. *Ocean Modelling*, *63*, 21–29.

Pelling, H. E., Uehara, K., & Green, J. M. (2013a). The impact of rapid coastline changes and sea level rise on the tides in the Bohai Sea, China. *Journal of Geophysical Research: Oceans*, *118*(7), 3462–3472. https://doi.org/10.1002/jgrc.20258

Pickering, M. D., Wells, N. C., Horsburgh, K. J., & Green, J. A. M. (2012). The impact of future sea-level rise on the European Shelf tides. *Continental Shelf Research*, *35*, 1–15.

Pous, S., Carton, X., & Lazure, P. (2012). A process study of the tidal circulation in the Persian Gulf. *Open Journal of Marine Science*, *2*(04), 131–140.

Pugh, D. (2004). *Changing sea levels: effects of tides, weather and climate*, Cambridge, UK: Cambridge University Press.

Rasheed, A. S., & Chua, V. P. (2014). Secular trends in tidal parameters along the coast of Japan. *Atmosphere-Ocean*, *52*(2), 155–168.

Rautenbach, C., Barnes, M. A., & de Vos, M. (2019). Tidal characteristics of South Africa. *Deep Sea Research Part I: Oceanographic Research Papers*, *150*, 103079.

Ray, R. D. (2001). Comparisons of global analyses and station observations of the S2 barometric tide. *Geophysics Research Letter*, *28*, 21–24. https://doi.org/10.1016/S1364-6826(01)00018-9

Ray, R. D. (2006). Secular changes of the M2 tide in the Gulf of Maine. *Continental Shelf Research*, *26*(3), 422–427. https://doi.org/10.1016/j.csr.2005.12.005

Ray, R. D. (2009). Secular changes in the solar semidiurnal tide of the western north Atlantic Ocean. *Geophysical Research Letters*, *36*, L19601. https://doi.org/10.1029/2009GL040217

Ray, R. D. (2013). Precise comparisons of bottom-pressure and altimetric ocean tides. *Journal of Geophysical Research: Oceans*, *118*(9), 4570–4584. https://doi.org/10.1002/jgrc.20336

Ray, R. D., & Foster, G. (2016). Future nuisance flooding at Boston caused by astronomical tides alone. *Earth's Future*, *4*(12), 578–587. https://doi.org/10.1002/2016EF000423

Robertson, R., & Ffield, A. (2008). Baroclinic tides in the Indonesian seas: Tidal fields and comparisons to observations. *Journal of Geophysical Research*, *113*(C7).https://doi.org/10.1029/2007JC004677

Ross, A. C., Najjar, R. G., Li, M., Lee, S. B., Zhang, F., & Liu, W. (2017). Fingerprints of sea level rise on changing tides in the Chesapeake and Delaware Bays. *Journal of Geophysical Research: Oceans*, *122*(10), 8102–8125. https://doi.org/10.1002/2017JC012887

Shankar, D. (2000). Seasonal cycle of sea level and currents along the coast of India. *Current Science*, *78*(3), 279–288. http://drs.nio.org/drs/handle/2264/31

Sharples, J., Tweddle, J. F., Mattias Green, J. A., Palmer, M. R., Kim, Y. N., Hickman, A. E., et al. (2007). Spring-neap modulation of internal tide mixing and vertical nitrate fluxes at a shelf edge in summer. *Limnology & Oceanography*, *52*(5), 1735–1747.

Sindhu, B., & Unnikrishnan, A. S. (2013). Characteristics of tides in the Bay of Bengal. *Marine Geodesy*, *36*(4), 377–407.

Stammer, D., Ray, R. D., Andersen, O. B., Arbic, B. K., Bosch, W., Carrère, L., et al. (2014). Accuracy assessment of global barotropic ocean tide models. *Reviews of Geophysics*, *52*(3), 243–282.

Sweet, W. V., & Park, J. (2014). From the extreme to the mean: Acceleration and tipping points of coastal inundation from sea level rise. *Earths Future*, *2*(12), 579–600. https://doi.org/10.1002/2014EF000272

Unnikrishnan, A. S. (2010). Tidal propagation off the central west coast of India. *Indian Journal of Geo-Marine Sciences*, *39*(4), 485–488.

Unnikrishnan, A. S., Kumar, K. R., Fernandes, S. E., Michael, G. S., & Patwardhan, S. K. (2006). Sea level changes along the Indian coast: Observations and projections. *Current Science*, *90*(3), 362–368.

Vellinga, N. E., Hoitink, A. J. F., van der Vegt, M., Zhang, W., & Hoekstra, P. (2014). Human impacts on tides overwhelm the effect of sea level rise on extreme water levels in the Rhine–Meuse delta. *Coastal Engineering*, *90*, 40–50.

Watson, P. J. (2011). Is there evidence yet of acceleration in mean sea level rise around mainland Australia?. *Journal of Coastal Research*, *27*(2), 368–377.

White, N. J., Haigh, I. D., Church, J. A., Koen, T., Watson, C. S., Pritchard, T. R., et al. (2014). Australian sea levels—trends, regional variability and influencing factors. *Earth-Science Reviews*, *136*, 155–174.

Woodworth, P. L. (2010). A survey of recent changes in the main components of the ocean tide. *Continental Shelf Research*, *30*(15), 1680–1691. https://doi.org/10.1016/j.csr.2010.07.002

Woodworth, P. L., Aman, A., & Aarup, T. (2007). Sea level monitoring in Africa. *African Journal of Marine Science*, *29*(3), 321–330.

Woodworth, P. L., Hunter, J. R., Marcos, M., Caldwell, P., Menéndez, M., & Haigh, I. (2016). Towards a global higher-frequency sea level dataset. *Geoscience Data Journal*, *3*(2), 50–59. https://doi.org/10.1002/gdj3.42

Wu, Z., & Huang, N. E. (2009). Ensemble empirical mode decomposition: A noise-assisted data analysis method. *Advances in Adaptive Data Analysis*, *1*(01), 1–41.

Zaron, E. D., & Jay, D. A. (2014). An analysis of secular change in tides at open-ocean sites in the Pacific. *Journal of Physical Oceanography*, *44*(7), 1704–1726.